The Astrophysical Journal, 941:160 (18pp), 2022 December 20 https://doi.org/10.3847/1538-4357/aca29a

Implications of High-density, High-temperature Ridges Observed in Some Two-ribbon Flares

Dana Longcope and Jiong Qiu
Department of Physics, Montana State University, Bozeman, Montana 59717, USA
Received 2022 August 26; revised 2022 November 11; accepted 2022 November 12; published 2022 December 20

Abstract

Several two-ribbon solar flares observed on the disk, notably including the Bastille flare of 2000 July 14, show an extended ridge of plasma running along the loop tops of the post-reconnection arcade. In that and two more recent examples, the ridge is visible in emission by Fe XXIV at roughly 17 MK, with a high, steadily increasing emission measure suggesting an expanding column of very dense plasma. We find that ridges are consistent with overhead views of long, vertical plasma sheets, such as seen above certain limb flares. Those vertical features show enhanced temperature and density over their entire lengths, making explanations in terms of termination shocks and evaporation collision seem less plausible. We use observations of several ridge events to argue in favor of compression and heating by slow magnetosonic shocks in the reconnection outflow. In this scenario, the ridge is built up as retracting flux piles hot, compressed plasma atop the post-flare arcade. Thanks to the overhead perspective offered by the ridge observations, we are able to measure the reconnection rate and show it to be consistent with the rate of increase in column emission measure across the ridge. This consistency supports the hypothesis that slow shocks and retraction compress the plasma seen in ridges, vertical plasma sheets, and possibly the high-temperature fans through which post-reconnection downflows are observed. Such a unified picture of these diverse features enhances our understanding of the role played by magnetic reconnection in solar flares.

Unified Astronomy Thesaurus concepts: Solar flares (1496)

1. Introduction

Elements of the accepted reconnection-driven solar flare model are supported by evidence found in a variety of observational signatures. According to the model, reconnection occurs in a global current sheet (CS) whose presence is inferred from images of certain limb flares in soft x-ray (SXR) and extreme ultraviolet (EUV; Savage et al. 2010; Liu et al. 2013). A notable example is offered by the X8 flare on 2017 September 10 (SOL2017-09-10T16:06) whose long-lived, hot, dense plasma sheet clearly resembles the CS expected to form in the wake of an eruption (Seaton et al. 2017; Doschek et al. 2018; Gary et al. 2018; Polito et al. 2018a, we refer to this well-studied plasma sheet as SEPT10PS). In the model, outflows at or near the Alfvén speed carry flux away from the reconnection site. Evidence for these flows is found in moving features, called supra-arcade downflows (SADs; McKenzie & Hudson 1999; Innes et al. 2003; Sheeley Jr. et al. 2004; McKenzie & Savage 2009), and/or SAD loops (SADLs) found in SXR and EUV images, including in SEPT10PS (Longcope et al. 2018). Footpoints of the reconnected field lines form a chromospheric flare ribbon in each magnetic polarity. The footpoints appear to sweep across the photospheric magnetic field at speeds determined by the rate of magnetic reconnection ($\dot{\Phi}$) occurring in the CS (Forbes 2000; Fletcher & Hudson 2001; Qiu et al. 2002). Finally, energy flux to the footpoints drives chromospheric evaporation, which is directly observed spectroscopically (Antonucci & Dennis 1983; Milligan & Dennis 2009; Graham et al. 2015; Li et al. 2015) and indirectly inferred through density enhancement of the coronal plasma (Dennis & Zarro 1993; McTiernan et al. 1999; Veronig et al. 2005; Qiu 2021).

Models also predict heating and compression of the coronal plasma through a variety of shocks, but evidence supporting them is less widely accepted. Outflows that exceed the local fast-magnetosonic speed will terminate at a fast-mode termination shock (FMTS; Forbes 1986). Direct evidence of such shocks has been found in observations in the radio and microwave (Aurass et al. 2002; Chen et al. 2015), and the EUV (Polito et al. 2018b). An upward slow magnetosonic shock is predicted to lead the chromospheric evaporation when it is abruptly initiated (Longcope 2014), although little observational evidence has been found for it. The fast reconnection model of Petschek predicts that the outflow is bounded by slow magnetosonic shocks (SMSs; Petschek 1964; Soward 1982; Lin & Lee 1999). These shocks have been invoked to explain the very high density over the length of SEPT10PS (Longcope et al. 2018).

Concentration of hot, dense plasma observed at the tops of reconnected loops (or the bottom of the CS) may offer further insight into some of these shocks. One version is the superhot ($\gtrsim$30 MK) thermal hard X-ray (HXR) sources observed at or above flare loops (Lin et al. 1981; Kosugi et al. 1994; Masuda et al. 1994). Thermalizing the superhot electron population requires very high density, typically $\gtrsim 10^{11}\,\mathrm{cm}^{-3}$, often consistent with emission measures (EMs) found in these sources (Jiang et al. 2006; Veronig et al. 2006; Caspi & Lin 2010). EUV imaging and spectroscopy show high-density concentrations atop flare loops, albeit at slightly lower temperatures ($T_e \sim 15$–20 MK Warren et al. 1999; Polito et al. 2018b).

Observed densities and confined pressures of these loop-top concentrations can be explained through some of the shocks posited by flare models. One possibility would be for the FMS

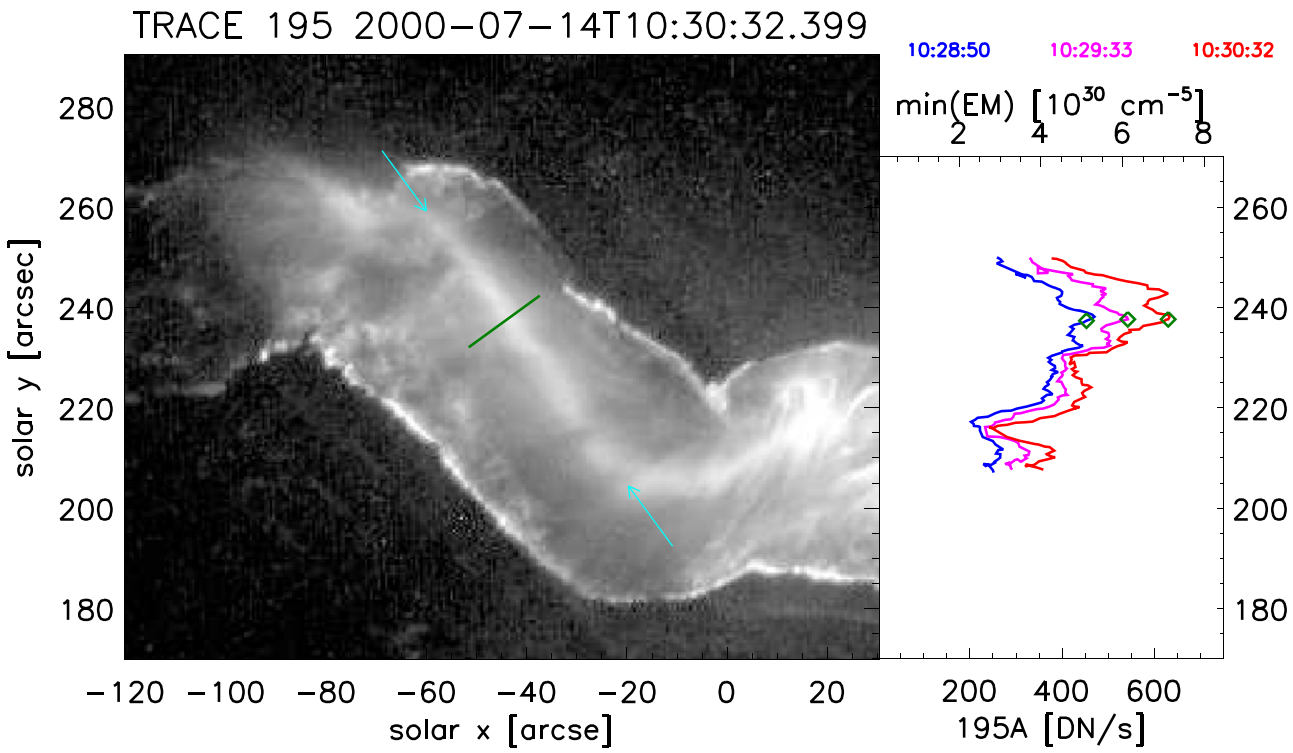

Figure 1. The hot, dense ridge observed by TRACE in the Bastille Day flare 2000. The left panel shows an image in 195 Å on a logarithmic gray scale. Cyan arrows indicate a line along which the ridge was sampled and plotted along the right in red. Samples from two previous times are shown blue and magenta. The bottom axis gives the values in data number per second and the top axis converts this to a minimum EM, as described in the text. Green diamonds mark the value found along the green slice denoted on the image.

to play this role, but the fast-magnetosonic Mach numbers one expects ($M \sim 1.5$–2) would produce only modest density enhancement (Forbes 1986). Simulations of flaring loops have shown loop-top SMSs caused by the collision of chromospheric evaporation from opposing footpoints (Reeves et al. 2007; Sharma et al. 2016). This evaporation-collision mechanism has been proposed to explain observed loop-top sources. While evaporation flows are typically observed to be subsonic (Unverferth & Longcope 2018), they are often supersonic in simulations and thus produce shocks upon collision. Supersonic though it may be, the evaporation has only a modest acoustic Mach number ($M \sim 2$, Fisher 1989; Longcope 2014) and will produce only modest density enhancement: Reeves et al. (2007) and Sharma et al. (2016) each find $n_e \sim 2 \times 10^{10}\,\mathrm{cm}^{-3}$ between their simulated loop-top shocks. Furthermore, the shocks move away from the collision at several hundred kilometers per second, causing the source to expand rapidly and fade.

The SMSs from Petschek's mechanism provide an alternative explanation for hot, dense loop-top concentrations, offering several advantages over FMTS or evaporation collision. A series of recent investigations have used the thin flux tube (TFT) approximation to simulate the outflow of retracting flux from flare reconnection (Longcope & Des 2010; Longcope & Guidoni 2011; Longcope et al. 2016). As in the skewed Petschek model, the shocks in the TFT model are caused by the collision of flows parallel to the field line generated by two rotational discontinuities (RDs) at the edge of the outflow region. The RDs generate Alfvénic flows whose acoustic Mach number is far higher than evaporation flows, thereby generating higher post-shock temperatures and densities. Retraction halts at the end of the outflow jet through force from the FMTS or from the underlying post-flare arcade. Since this force is perpendicular to the field, it has a limited effect on the parallel flows, which therefore continue to maintain the SMSs at the top of the now-stationary post-flare loop. This persistent confinement on post-flare loops piling atop one another has been shown to produce a loop-top source of size and EM consistent with particular observations (Longcope et al. 2016).

A possible means of identifying the particular shock responsible may be offered by the novel observational constraint found in a *ridge* of hot plasma sometimes seen in EUV images of two-ribbon flares observed on the disk. The prototypical example of such a ridge was observed in the Transition Region And Coronal Explorer (TRACE; Handy et al. 1999) 195 Å images of the flare on 2000 July 14 (the so-called Bastille Day flare) shown in Figure 1. The ridge is a bright, narrow (width of about 4 Mm), somewhat diffuse curve falling between the more sharply defined flare ribbons. A particularly straight section is called out by cyan arrows in the figure. Its general appearance suggests the feature is emitting in Fe XXIV formed at $T \simeq 17$ MK (Warren et al. 1999), and it is therefore probably located along the top of the post-flare arcade. We use this assumption to place a lower bound on the ridge's column EM, plotted along the right. The large EMs ($\mathrm{EM} \gtrsim 6 \times 10^{30}\,\mathrm{cm}^{-5}$) suggest very large densities, akin to those ascribed to loop-top sources discussed above.

While hot ridge structures of this kind may differ from more common loop-top sources, they have been frequently explained through one of the same shock mechanisms used for those features. They may, however, offer additional evidence in favor of one among these possible mechanisms, owing to their coherent structure, time evolution, and amenability to magnetic

modeling. To our knowledge, no dedicated study has been focused on explaining them; this will be our objective.

The density and temperatures of ridges are found to roughly match those inferred for vertical plasma sheets observed above some limb flares, notably SEPT10PS (Doschek et al. 2018; Li et al. 2018; Warren et al. 2018). Like the ridges, SEPT10PS was visible through ∼17 MK emission of Fe XXIV in 193 Å images of the Atmosphere Imaging Assembly (AIA; Lemen et al. 2012). The sheets are long and narrow: Seaton & Darnel (2018) used GOES' SUVI imager to trace that particular sheet out to 1.67 $R_\odot$; Longcope et al. (2018) used AIA 193 Å images to measure its width as narrow as 4 Mm. Associating these vertical features, observed on the limb, with ridges seen on the disk seems problematic in light of extents exceeding 100 Mm: it would seem to require an extremely fortuitous perspective for a 100 Mm long sheet to appear as a ridge ∼5 Mm wide. We find, however, that the vast majority of the emission from SEPT10PS originates from a very low section. We go on to propose that plasma ridges observed from overhead are, in fact, the same structures as vertical plasma sheets viewed on the limb from edge on.

Our proposed association is only a starting point since there is not yet an accepted explanation for the very high densities observed in plasma sheets. Since temperature and density enhancement occurs along the entire sheet, FMTS and evaporation collision seem less plausible: each predicts a concentrated source. Longcope et al. (2018) posited that plasma compression by SMSs within the flux retracting following reconnection could produce the observed level of density enhancement along the entire sheet. A steady increase in column EM could be explained by the increasing mass of shocked material combined with compression through retraction into increasing field strength. The overhead perspective offered in ridge observations allows reconnection to be measured from the motion of the flare ribbons, permitting this reconnection-compression hypothesis to be subjected to a new test.

The present investigation characterizes three well-observed examples of ridges with the aim of understanding the origin of this feature, and thereby of vertical plasma sheets. Each case we consider has a phase in which the column EM grows linearly in time for 3–4 minutes, reaching a value of around 3×10^{30} cm^{-5}. This is shown to be consistent with a buildup of plasma at the base of a vertical plasma sheet. Indeed, we are able to relate the rate of reconnection, measured through outward ribbon motion, to the upward expansion of the ridge. We find that, under this scenario, the retracted flux is carrying plasma whose electron density, $n_e \sim 7 \times 10^{10}$ cm^{-3}, is comparable to that found in the bases of vertical plasma sheets, such as SEPT10PS. Neither FMTS nor evaporation collision appears consistent with this scenario. We conclude that the compression leading to both the plasma sheet and the high-density ridge is best explained through SMSs within the reconnection outflow.

The investigation is presented as follows. The next section outlines three cases of observed ridges, and the data used to analyze each one. In each case, a magnetic model is constructed to help with the analysis. Two cases were observed in multiple EUV bands by SDO/AIA, which we use to derive column EM and temperature along the ridge. Section 3 describes the properties and evolution of a typical ridge by analyzing the data from each case. In Section 4, the properties are collected into a coherent picture of the ridge and its formation. Here, we present a detailed argument that a ridge is the same structure as the vertical plasma sheet, but observed from overhead. The final section discusses what our analysis of ridges may reveal about the vertical plasma sheet, and other observational features such as supra-arcade fans.

2. Flare Observation Featuring Hot, Dense Ridges

Hot, dense ridges appear clearly in a small number of large, two-ribbon flares. In an effort to establish those properties common to the phenomenon in general, we consider three different flares exhibiting ridges, which we hereafter refer to as FLARE2000, FLARE2021, and FLARE2014. Figure 2 summarizes the three flares and the data used to analyze each one, as well as the figures in this work used to present the analysis. Each case has its own peculiarities, data availability, and its observations suffer from particular limitations. They can be combined to reveal the general properties of the phenomenon. The analysis of each is described in detail below.

2.1. FLARE2000: The Bastille Day Event

The prototypical case of a high-density ridge is that from the X6 class flare and associated eruption on 2000 July 14 (SOL2000-07-14T10:24), often called the Bastille Day flare. It is a two-ribbon flare accompanying two distinct phases of filament eruption (Fletcher & Hudson 2001). In the second phase, beginning at 10:24 UT, the eastern portion of the filament erupted, producing an arcade in which the hot ridge is most evident in TRACE 195 Å images made at high cadence (see Figure 1). To study the ridge we focus exclusively on the second phase and on the eastern portion of the eruption and refer to this case hereafter as FLARE2000. The ridge is visible in 195 Å by 10:26:47, just after TRACE left the South Atlantic Anomaly. Arcade loops begin to appear across the ridge around 10:37:13, making it difficult to identify the latter after that time.

The ridge of FLARE2000 is analyzed using the high-cadence observations made by TRACE in 195 Å. We discard those images which are erroneously ascribed to this band (Aschwanden & Alexander 2001), and compensate for a few that appear to have erroneously reported exposure times. We extract the ridge pixels by searching vertically for peak intensity from positions along the line indicated by the cyan arrows on the left of Figure 1. These values are plotted at three representative times along the right panel.

The TRACE 195 Å bandpass is dominated by contributions from Fe XII and Fe XXIV whose peak formation temperatures are 1.5 and 17 MK, respectively. Based on its smooth, diffuse morphology, we interpret the emission from the ridge in Figure 1 as being from Fe XXIV at $T \simeq 17$ MK. The top axis along the right panel shows the minimum column EM required to produce the observed intensity from such emission. To obtain this value we divide the observed intensity, in data number per second, by the high-temperature peak in the response function, $\max(R_\lambda) = 8.9 \times 10^{-29}$ DN cm^5 px^{-1} s^{-1}, reported by `trace_t_resp` in the SolarSoft distribution (SSW; Freeland & Handy 1998). A later image from this band, shown on the left of Figure 3, exhibits clearly defined loops, which we attribute to emission from the cooler Fe XII. Along the right, the EM is estimated by dividing the intensity by a lower-temperature peak in the response function, $\max(R_\lambda) = 4.8 \times 10^{-27}$ DN cm^5 px^{-1} s^{-1}. Although that image is from

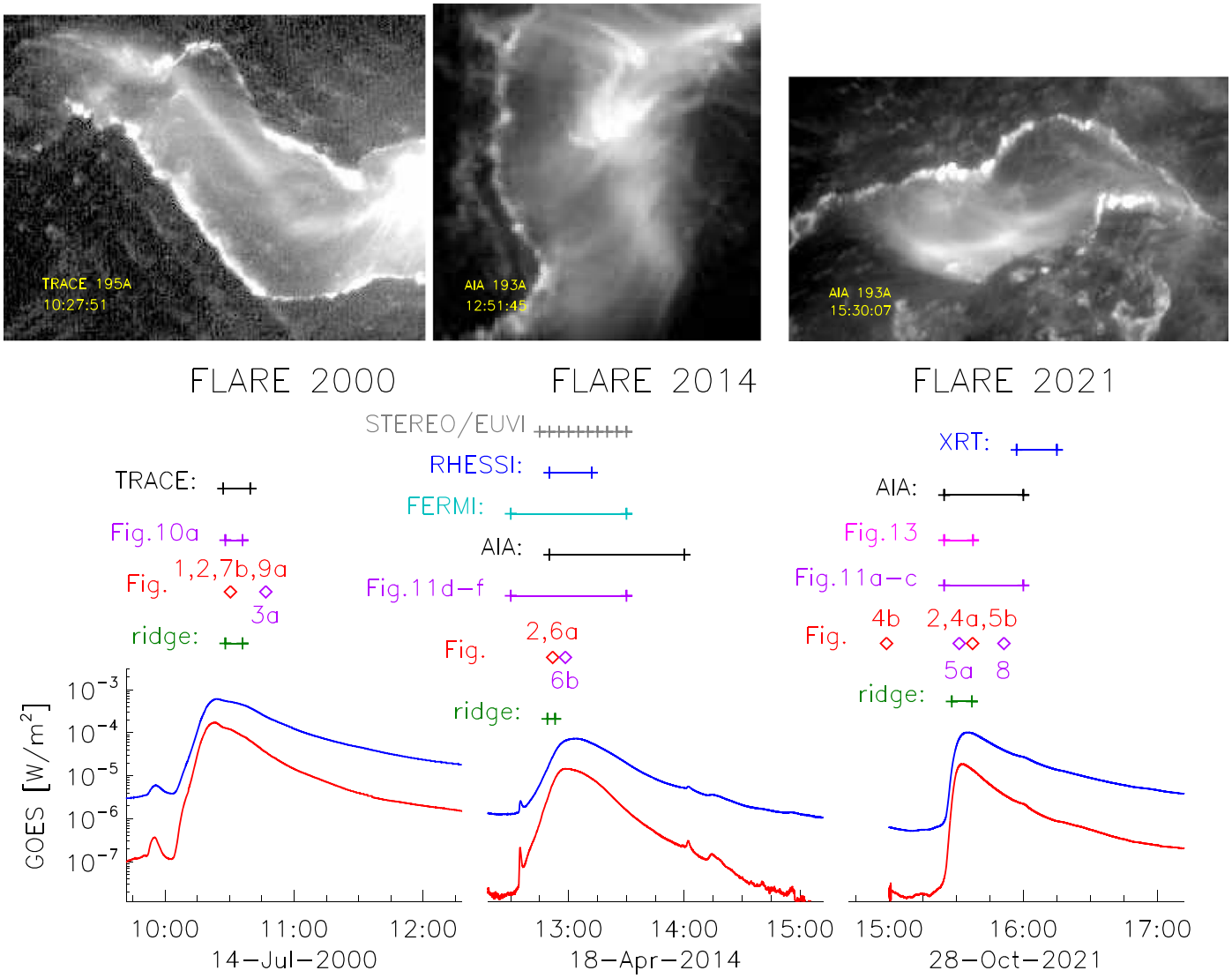

Figure 2. Summary of the three flares exhibiting ridges examined in this work. The bottom panel shows timelines for each flare, including GOES Lo (blue) and Hi (red) channels. Symbols and bars above these are a preview of the data used to analyze each flare, and the times of the figures featuring that data. Thumbnail images of the ridge appear above each timeline.

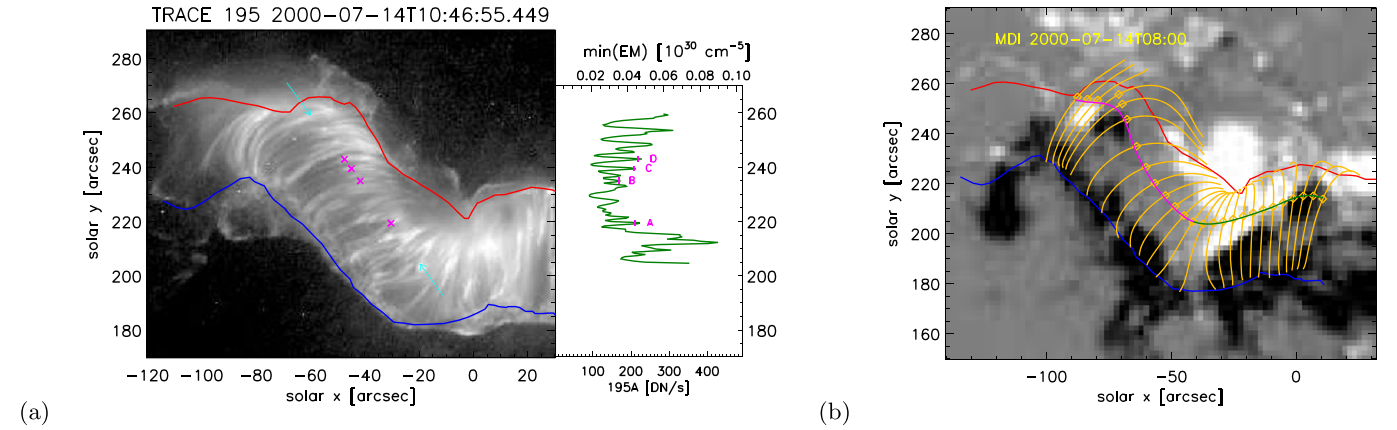

Figure 3. The post-flare arcade and a magnetic model of it. (a) TRACE 195 Å image from later in the flare shown in logarithmic gray scale. Red and blue curves represent the flare ribbons visible earlier (Figure 1) and cyan arrows are repeated from that figure. The green curve along the right shows the intensity between the arrows, with four peaks, representing loops, called out with magenta ×s. (b) gray scale showing a line-of-sight magnetogram from SoHO/MDI before the flare (8:00). Red and blue curves represent the ribbons repeated from (a). Orange curves denote representative field lines, with orange diamonds at their midpoints. The magenta and green curves trace their apexes.

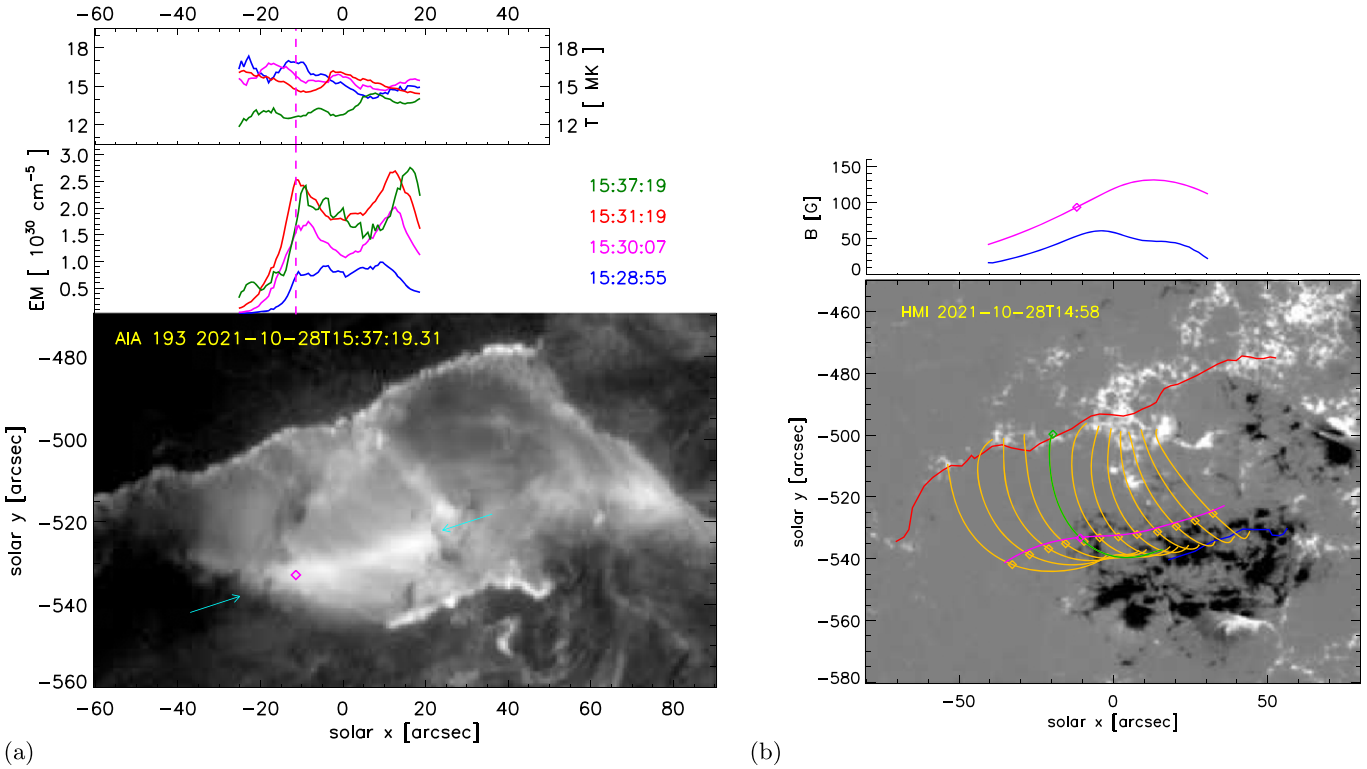

Figure 4. Observations of FLARE2021 by SDO. (a) an image from the 193 Å band of AIA at 15:37:19, rendered with logarithmic gray scale. Cyan arrows indicate the ridge and a red diamond calls out a ridge pixel used in subsequent figures. Axes along the top plot T (top) and EM (middle) along the ridge at that time (green) and three earlier times. (b) The HMI line-of-sight image from before the flare (14:58) plotted in gray scale. Elements of the magnetic model using the format from Figure 3(b). The magenta curve traces the locus of field lines apexes. The magenta diamond is the same reference pixel, linked now to a green field line. The value of $|\boldsymbol{B}|$ along the magenta apex curve is plotted in magenta in the top panel. The blue curves show the component of $\boldsymbol{B}$ parallel to that curve—analogous to the guide field.

16 minutes later than the image showing the ridge (Figure 1) the cool loops it shows appear anchored along the ribbons from the earlier view (blue and red curves), so we interpret them as a relaxed version of the loops being reconnected at the earlier time.

We construct a relatively crude magnetic model of the post-flare arcade from a pre-flare (8:00 UT) line-of-sight magnetogram from the Michelson Doppler Imager (MDI; Scherrer et al. 1995) on board SoHO. We project the magnetogram onto the tangent plane from 10:30, assuming the line-of-sight field to be a component of a purely radial field, and extrapolating a constant alpha field upward. The arcade with apex height h is found by tracing those field lines originating in the curve defined by $B_z(x, y, h) = 0$, shown as magenta and green curves on the right of Figure 3. We find that choosing $\alpha = -1.6 \times 10^{-10}\,\mathrm{cm}^{-1}$ and $h = 26.2$ Mm yields an arcade of field lines mostly anchored near the ribbon (red and blue curves) and sheared to a similar extent as those between the cyan arrows in Figure 3.

2.2. *FLARE2021: X1 Flare on 2021 October 28*

An X1 flare on 2021 October 28 (SOL2021-10-28T15:35), hereafter called FLARE2021, has a two-ribbon structure resembling the prototypical case, but with the advantage of imaging data in more EUV bands. The flare occurs near the central meridian, but at 26° S it remains rather far from the disk center. Images made by SDO/AIA in three bands with a high-temperature response (193, 131, and 94 Å) show a ridge, typified by the 193 Å image in Figure 4. Like the TRACE 195 Å band discussed above, the AIA 193 Å band shows contributions from Fe XII and Fe XXIV, and we show below that the ridge in that image is from the hotter line ($T \simeq 17$ MK). We use only those 193 and 131 Å images with shortened exposure times since they do not suffer from saturation. We used `aia_prep` from the SSW (Freeland & Handy 1998) and verified coalignment using the flare ribbons. The ridge becomes evident in 193 Å images beginning about 15:28:31. Absorbing filament material moves northward and beginning around 15:32:07 it begins to obscure the ridge, making analysis difficult. By 15:35:18 the ridge becomes mostly clear again (see Figure 4(a)), and persists until 15:39:19 when 193 Å images begin to show mostly arcade loops.

The multiple imaging bands of SDO/AIA make it possible to use a simplified EM-loci technique (Landi et al. 2002) to compute temperature and EM along the ridge. A given pixel, i, such as that identified by a diamond in Figure 4, will be characterized by an intensity $I_{\lambda,i}$ for each band λ. A pair of such intensities $I_{\lambda,i}$ and $I_{\lambda',i}$, defines an EM_i and temperature T_i by satisfying

$$\frac{I_{\lambda,i}}{R_\lambda(T_i)} = \frac{I_{\lambda',i}}{R_{\lambda'}(T_i)} = \mathrm{EM}_i \ , \qquad (1)$$

for the quoted response function of each band, $R_\lambda(T)$ and $R_{\lambda'}(T)$ (these are obtained from the `aia_get_response` in SSW). For the pair $\lambda = 193$ and $\lambda' = 131$ Å we generally find two intersections, as between the blue and red curves in Figure 5. The blue curve has a local minimum at $T = 11$ MK, corresponding to the peak in $R_{131}(T)$ from Fe XXI. Two minima in the 193 Å (red) curves are created by the two peaks in $R_{193}(T)$ discussed above: one at $T = 17$ MK, from Fe XXIV

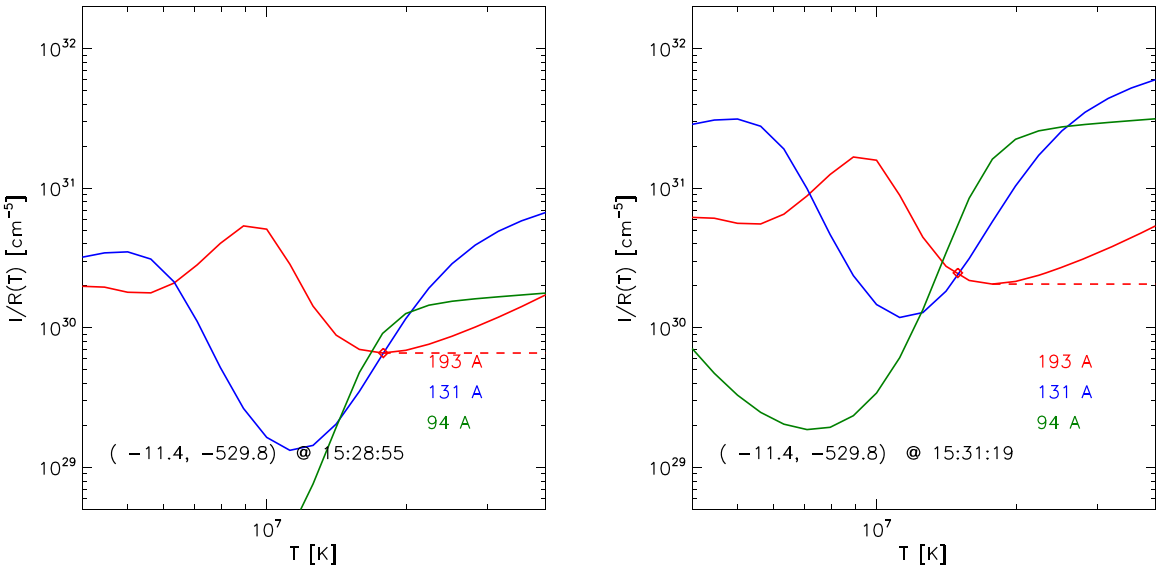

Figure 5. The simplified EM-loci technique used to compute EM_i and T_i for a single pixel of FLARE2021 at two different times. The ratio $I_{\lambda,i}/R_\lambda(T)$ is plotted vs. T for $\lambda = 193$Å (red), $\lambda = 131$Å (blue), and $\lambda = 94$Å (green). The hotter intersection of red and blue curves, called out by the red diamond, determines the value of EM_i and T_i for that pixel. The red dashed lines show the lower bound on EM_i one obtains if only the 193 Å image is available, as in FLARE2000.

(right), and another $T = 1.5$ MK from Fe XII (not visible). The hotter intersection, indicated by a red diamond, is the one approximating an intersection with $\lambda' = 94$ Å (green curves). We find this to be consistently true along the ridge, and therefore use the hotter intersection between $\lambda = 193$ Å and $\lambda' = 131$ Å to set EM_i and T_i.

As with FLARE2000, ridge pixels are taken as those with maximum intensity along the vertical line. For each such pixel, we use the hotter intersection of red and blue curves (i.e., $\lambda = 193$ Å and $\lambda' = 131$ Å) to compute EM_i and T_i. These values along the ridge, at four different times, are plotted on the axes above the 193 Å image of Figure 4. The dashed vertical line is the pixel indicated by the diamond, and the one used to illustrate the simplified EM-loci technique in Figure 5.

A magnetic model is constructed using the same steps described in the foregoing section. A line-of-sight magnetogram from the Helioseismic and Magnetic Imager (HMI; Scherrer et al. 2012) is projected onto the tangent plane and extrapolated upward with $\alpha = +2.8 \times 10^{-10}\,\mathrm{cm}^{-1}$. With this value, field lines with apexes at $h = 19.9$ Mm appear anchored mostly along the ribbons from 15:37:19, are sheared to match loops visible in 193 Å about 19 minutes later, and have similar footpoints.

2.3. FLARE2014: M7 Flare on 2014 April 18

To provide contrast, we consider the well-studied, eruptive M7 flare on 2014 April 18 (SOL2014-04-18T13:03, Brannon et al. 2015; Brosius & Daw 2015; Brosius et al. 2016). In addition to the multiple bands of AIA images, this flare has HXR data from the Reuven Ramaty High Energy Solar Spectroscopic Imager (RHESSI; Lin et al. 2002), showing footpoint sources in 25–50 keV HXR emission (see Figure 6(b)). The flare ribbons are fairly complex, running north–south in the region and then to the west. The Interface Region Imaging Spectrograph (IRIS; De Pontieu et al. 2014) observed the flare, but its spectral slit observed only the western section, away from the ridge and HXR sources. The 193 Å image in Figure 6(a) shows a hot ridge, although not as obviously as in the other two cases. Ridge pixels are extracted and subject to the simplified EM-loci techniques, described above, to obtain EM and T values, plotted along the right axis of Figure 6(a). This example has EM lower than the other two cases.

The magnetic model is constructed using the same steps described above beginning with a line-of-sight magnetogram from SDO/HMI during the flare (12:58) projected onto the tangent plane. This is extrapolated upward with $\alpha = +0.41 \times 10^{-10}\,\mathrm{cm}^{-1}$. With this value, field lines with apexes at $h = 11.7$ Mm appear anchored mostly along the ribbons from 12:50, are sheared to match loops visible in 171 Å at 13:09, and have similar footpoints. The arcade is plotted over in orange the HMI magnetogram, with a particular field line called out in violet, whose feet are close to the HXR footpoints. The apex of this field line is indicated by a diamond on the field line, and repeated on the curves on EM and T in Figure 6(a).

3. Morphology and Evolution of Ridges

3.1. Proposed Location of Ridge

The general appearances of the ridges in the three flares considered here suggest they are produced by a horizontal column of hot, dense material located along the top of the post-flare arcade or the bottom of the reconnection CS (see Figure 7(a)). The first evidence supporting this interpretation is the apparent location of the ridge. In every case the EUV ridge appears between the opposing flare ribbons and runs approximately parallel to them. The magnetic models have been used to locate the curve of loop tops lying at a common height. When this curve is projected onto the plane of the sky it appears to follow the ridge, as shown for the case of FLARE2000 shown in Figure 7(b).

The ridges are notably straight, lacking the smaller-scale meanderings of the ribbons. The prototypical case, FLARE2000, was striking for the straightness of the section between the arrows of Figure 1. The brightest 42″ section of the ridge fits a parabolic curve with a radius of curvature greater than 2000″, and all intensity peaks fall within 1″ of it. The ridge remains roughly that smooth and straight until about 10:33:02, after

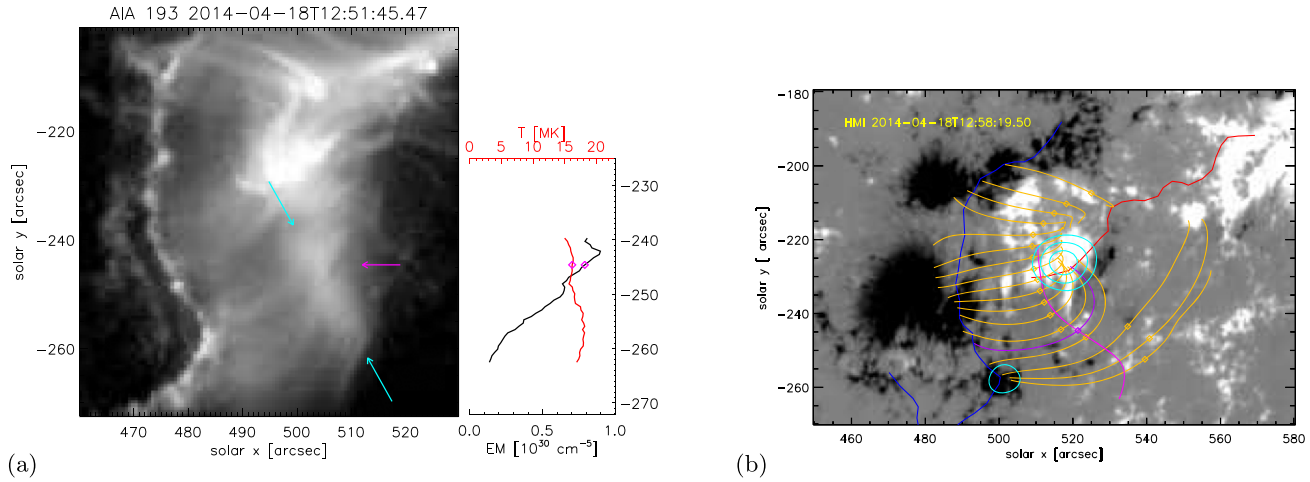

Figure 6. Images of the hot ridge of the 2014 April 18 flare and its magnetic model. (a) The image in 193 Å from 10:51:45 plotted using a logarithmic gray scale. Cyan arrows indicate the ridge, and a red arrow singles out a representative pixel. Curves of EM (black from bottom axis) and T (red from top axis) are plotted along the right. (b) The HMI line-of-sight image from 12:58 plotted in gray scale. Elements of the magnetic model using the format from Figure 3(b). Cyan contours show the HXR emission in the 25–50 keV band, at contour levels of 60%, 75%, and 90% of maximum.

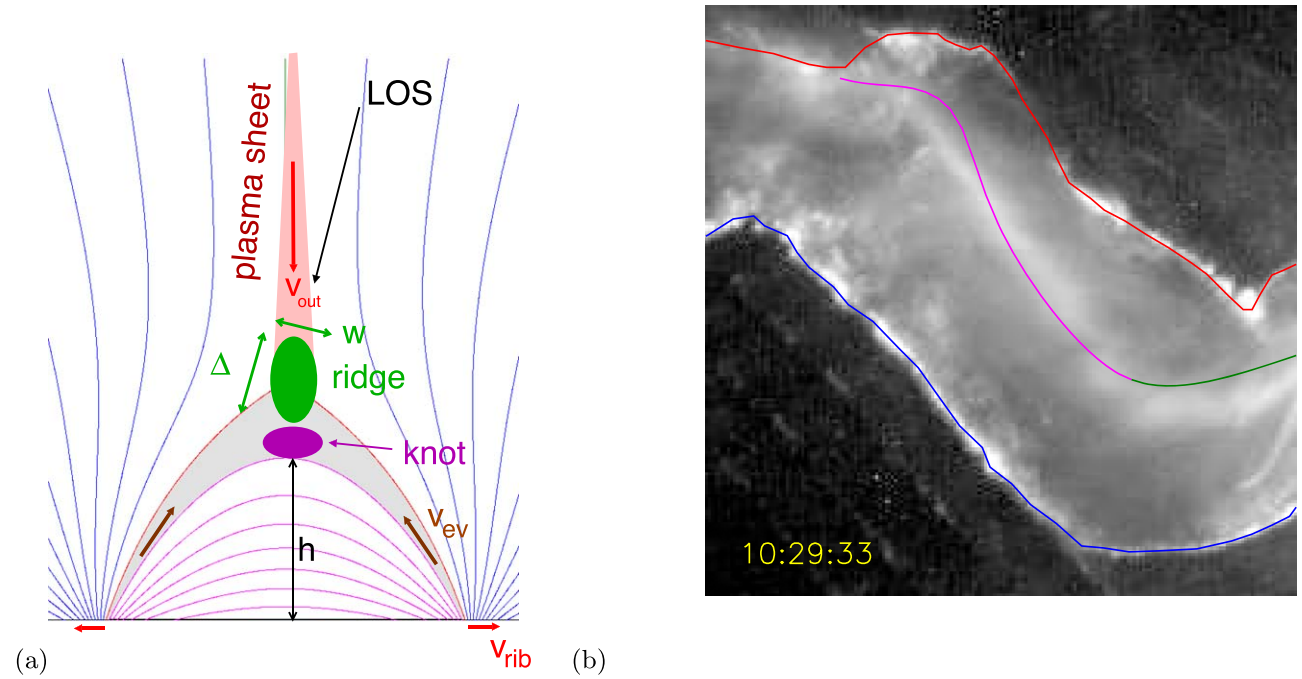

Figure 7. The proposed location of the ridge. (a) A schematic based on a two-dimensional CS in an otherwise current-free field. Reconnection occurring between open field lines (blue) creates closed flux, which is moved down by an outflow (pink) at $v_{\rm out}$ to form the post-flare arcade of height h (magenta). The ridge (green ellipse) occurs at the end of the outflow and top of the most recently reconnected flux tube (gray). The outward motion of the ribbons, at $v_{\rm rib}$ and evaporation at $v_{\rm ev}$ are indicated by red and brown arrows, respectively. Separate structures, called loop-top knots, form beneath the ridge, shown by a violet ellipse. (b) An image of the ridge on FLARE2000 similar to, but earlier than, Figure 1. Curves from Figure 3(b) are overplotted on the image: the curve of field line apexes at $h = 26.2$ Mm (magenta and green) and the flare ribbons (red and blue).

which loops appear, and intensity peaks begin to scatter away from the central curve. It is notable that the ridge of field line apexes, shown as the magenta curve in Figure 7(b), is not as straight as the actual ridge. The bright section of FLARE2021, shown between the arrows in Figure 4, is also very straight, with a 38″ stretch fitting a curve with 275″ radius of curvature, and all peaks falling within 0.″6.

3.2. Ridge Cooling and Loop-top Knots

In general, ridges cool over time until, at some point, the Fe XXIV emission ceases and the 193 or 195 Å images show instead mostly loops emitting in Fe XII. This transition occurs in all flares we consider, and is particularly evident in FLARE2000 through a comparison between Figures 1 and 3(a). The cooling itself is more explicit in the case of FLARE2021 where the top panel of Figure 4(a) shows that from 15:30 (magenta) to 15:37 (green) the central region dropped from $T = 17$ to 13 MK. Figure 8 shows that ridge even later (15:51:20) when the 193 Å image (Figure 8(a)) shows only the jagged tops of loops, but 131 and 94 Å images (Figures 8(b) and (d)) continue to show the ridge. There is no single intersection in the EM-loci plot, Figure 8(c), suggesting

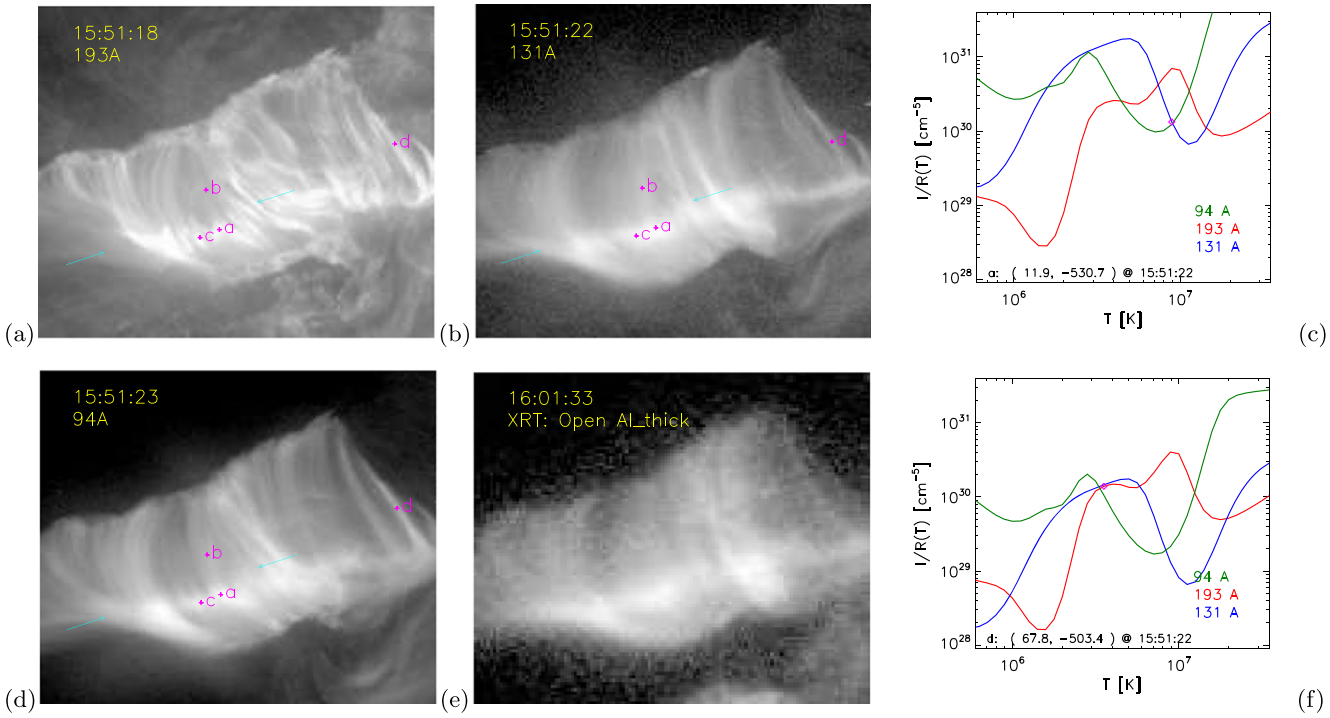

Figure 8. A phase later in FLARE2021, when the ridge has cooled. (a), (b), and (d) show AIA images in 193, 131, and 94 Å, respectively, at 15:51:20, using a logarithmic gray scale. Cyan arrows are repeated from Figure 4. Four pixels, labeled a–d are designated by magenta +s. (c) and (f) show the EM-locus plots for points a and d, using the same format as Figure 5. The magenta diamond is the proposed intersection. (e) Shows an image from XRT at an even later stage (16:01:33) also using a logarithmic gray scale.

that the ridge and loop tops are distinct features falling along the line of sight, but at different temperatures. Points b and c behave similarly, however, point d (Figure 3(f)) is a simple loop and all three curves intersect at a single point: $T = 3.5$ MK, $\mathrm{EM} = 1.4 \times 10^{30}\,\mathrm{cm}^{-5}$.

We propose that the 193 Å image (Figure 8(a)) shows cool, bright, loop-top knots, of the kind studied by Patsourakos et al. (2004). If these features are as cool as proposed by that team, then they dominate the 193 Å image, while contributing little to the other bands. Under this hypothesis, the intersection designated by a magenta diamond in Figure 8(c) ($T = 8.9$ MK, $\mathrm{EM} = 1.3 \times 10^{30}\,\mathrm{cm}^{-5}$) characterizes the ridge alone. The 193 Å contribution comes from a cooler loop-top knot, causing the red curve to pass above the diamond.

The ridge's smooth, straight morphology further supports our hypothesis that it is related to the CS and is not formed from a collection of knots atop independent flare loops. The example of FLARE2000 clearly makes this case through a comparison of curves along the right axes of Figures 1 and 3(a), which show the relatively large-scale intensity variation of the ridge (scales of 10″ or more), compared to the loops and their knots (a few arcseconds). Further evidence is found in the jaggedness that results from loop-confined knots (i.e., Figure 3(a)); even when neighbors are producing similar apex brightenings, they do not line up to form a straight smooth structure as does the ridge.

The distinction we propose is illustrated in Figure 7(a): the ridge occurs above the knots. The ridge is also hotter and more continuous along the base of the CS. The two structures do appear to be somehow related, but we defer investigation of this relation to future work, and confine our focus to the ridge.

The FLARE2021 ridge cools from $T = 16$ to 9 MK over the course of 10 minutes. It remains visible in 94 Å for at least another 15 minutes. The X-ray Telescope (XRT; Golub et al. 2007) on board Hinode observed the late phase of this flare, showing the ridge after 16:00, when it appears to have cooled further to $T = 5$ MK (Figure 8(e)). Loop-top knot structures begin to appear in each band. As these contribute to the images, the ridge becomes increasingly difficult to characterize in isolation. We hereafter restrict our study to the very early phase, when the ridge can be easily isolated.

3.3. Relation to Hot Loops

Extending from the bright, straight ridge are sometimes found subtle indications of equally hot loops intersecting it. Examples of these features, evident in both Figures 1 and 4, are isolated and called out in Figures 9(a) and (b). In Figure 9(c), the loops from Figure 9(b) are enhanced using an unsharp mask.[1] Their faintness and blending with the ridge suggest the loop segments are visible in 193–195 Å through Fe XXIV emission, like the ridge itself. They are short and particularly straight, unlike the later loops visible in Fe XII emission (see Figure 3(a)). A likely explanation is that the ∼15 MK plasma from the ridge is moving outward along at least a few loops.

In the case of FLARE2021 (Figure 9(b), (c)) the loop directions are notably different on opposite sides of the ridge. They make angles with the ridge of $\theta_N = 60°$ (green) and $\theta_S = 25°$ (magenta) on its north and south sides. Such a change in direction in the plane of the sky could be attributed to the three-dimensional geometry depicted in Figure 9(d), where straight loop segments meet at a vertex on the ridge. The figure

[1] To enhance high-wavenumber features, we subtract from the image a version that has been smoothed through convolution with an 11×11 pixel box-car filter. This process is known as unsharp masking (Deng 2011).

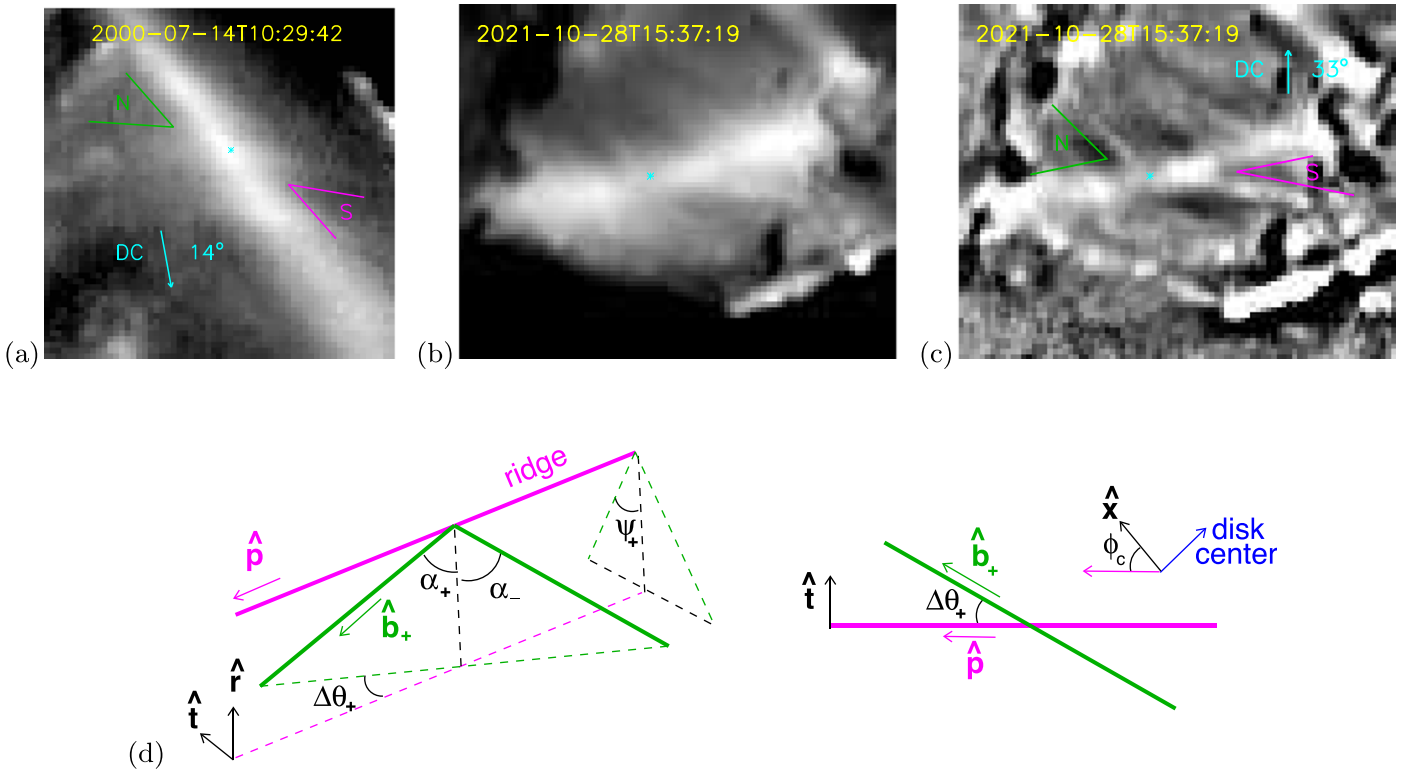

Figure 9. Sections of the ridges from (a) FLARE2000, and (b) FLARE2021, with pieces of loops visible. Image (b) is enhanced with an unsharp mask in (c). Notable features extend from the point indicated by a cyan asterisk. Angled lines to either side, labeled N and S, show the direction of the features and of the ridge. (d) The geometry of the ridge (solid magenta) and loop segments (solid green) used to interpret the images. A perspective view on the left has various angles and directions labeled, and projections depicted as dashed lines. The overhead view on the right shows the axis, $\hat{\boldsymbol{x}}$, about which the construction will be rotated to transform it into the plane of the sky.

shows them directed along

$$\hat{\boldsymbol{b}}_\pm \;=\; -\hat{\boldsymbol{r}}\cos\alpha_\pm \;\pm\; \sin\alpha_\pm\,[\hat{\boldsymbol{p}}\,\cos(\Delta\theta_\pm) \;+\; \hat{\boldsymbol{t}}\,\sin(\Delta\theta_\pm)\,]\;, \tag{2}$$

assuming the ridge is directed along the horizontal $\hat{\boldsymbol{p}}$. The vectors, $\hat{\boldsymbol{b}}_\pm$ and $\hat{\boldsymbol{p}}$, are transformed into the plane of the sky by rotating by the angular distance to the disk center, θ_c. The axis of rotation, $\hat{\boldsymbol{x}}$, makes an angle ϕ_c from $\hat{\boldsymbol{p}}$ as shown. From the transformed vectors we extract the components lying in the plane of the sky and compute the angle with respect to one another. The result is the apparent angles θ_+ and θ_- shown in green and magenta in Figures 9(a) and (c).

This analysis is applied to the cases of FLARE2000 and FLARE2021 shown in Figures 9(a)–(c). FLARE2000 is relatively close to disk center ($\theta_c = 14°$), leaving $\theta_\pm \simeq \Delta\theta_\pm \simeq 40°$. Little information about $\alpha_\pm$ can be obtained from this overhead perspective. Since FLARE2021 is further from the disk center ($\theta_c = 33°$) it does contain information about both $\Delta\theta$ and α. To obtain this we assume that $\Delta\theta_+ = \Delta\theta_-$ and $\alpha_+ = \alpha_-$. Under these assumptions, we may match the observations, $\theta_+ = 25°$ and $\theta_- = 60°$, with values $\alpha = 70°$ and $\Delta\theta = 35°$. With these values, the triangular arcade has a half angle $\psi = \tan^{-1}[\sin(\Delta\theta)\tan(\alpha)] = 58°$ (see Figure 9(d)).

Both flares show a magnetic field crossing beneath the CS at a strongly sheared angle—i.e., far from perpendicular ($\Delta\theta = 90°$). This is consistent with previous flare observations showing magnetic shear tends to be particularly high early in a flare. Of the magnetic field in each loop segment, the component parallel to the ridge accounts for a fraction

$$f_p \;=\; \frac{|B_p|}{|\boldsymbol{B}|} \;=\; |\,\hat{\boldsymbol{p}}\cdot\hat{\boldsymbol{b}}_\pm\,| \;=\; \sin(\alpha_\pm)\cos(\Delta\theta_\pm)\;, \tag{3}$$

after using Equation (2). This is related to the so-called guide field in the CS above the ridge. For FLARE2021, where $\alpha = 70°$ and $\Delta\theta = 35°$, the parallel fraction is $f_p \simeq 0.77$. For FLARE2000, we can say only that $f_p < \cos(\theta_\pm) = 0.77$.

3.4. Time Evolution and EM

All examples show a similar time evolution with the ridge brightening over the first few minutes. Figure 10 shows light curves and several slices from FLARE2000 (a) and FLARE2021 (b). In each panel, the peak emission (diamond) rises over the first 3–4 minutes at the same time it broadens or shifts at ∼10 km s^{-1}. The ridge on FLARE2021 (b) has an FWHM shown by triangles) of $w \simeq 4$ Mm, which does not change over that initial period. The peak moves down the image at $v_y \simeq -7.5$ km s^{-1}. If this were a purely radial motion, projected at $\theta_c = 33°$, the upward velocity would be $v_r = |v_y|/\sin(\theta_c) = 13.8$ km s^{-1}. In contrast to this, FLARE2000 (a) broadens steadily with the FWHM increasing from $w = 2.6$ Mm at 10:28:50 (blue) to $w = 3.2$ Mm at 10:30:32 (red); this is an average rate of $\dot{w} = 5.6$ km s^{-1}. While the peak location appears roughly fixed, the broadening occurs on the northwestern shoulder, which may be interpreted as radial motion, since the disk center is approximately due south.

A particularly noteworthy feature of all three ridges is that, at many of their points, the column EM increases linearly with

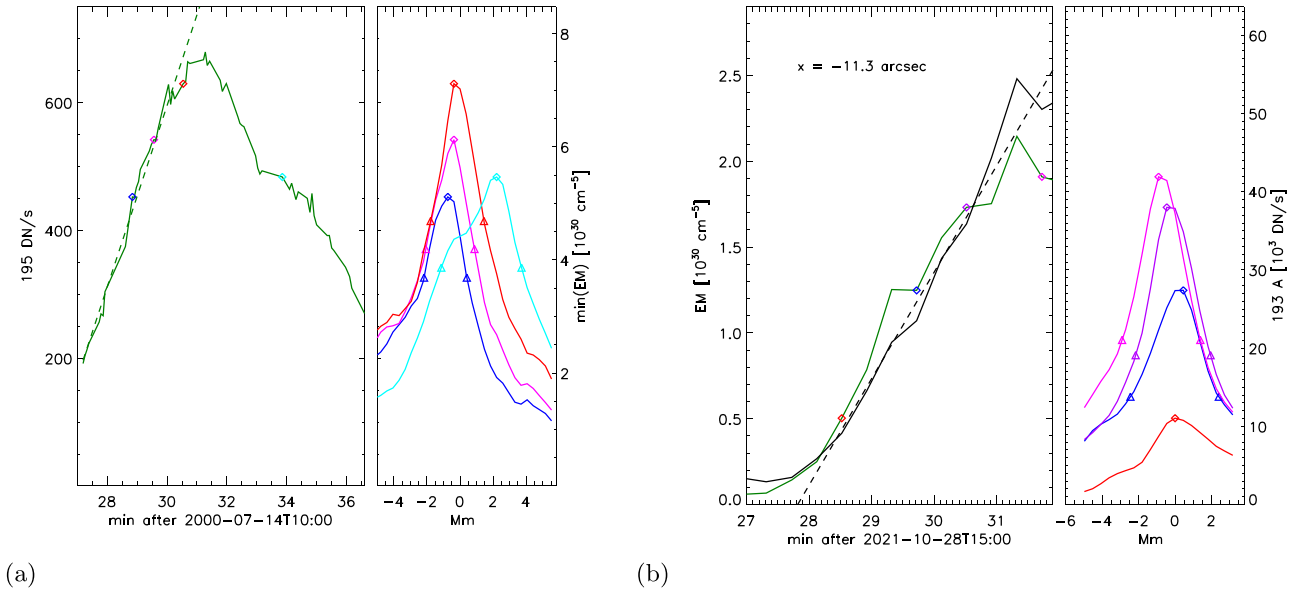

Figure 10. The evolution of intensity within ridges of FLARE2000 (a) and FLARE2021(b). The FLARE2000 ridge (a) is sampled along the green line from Figure 1. The left panel shows the time evolution of the peak intensity from that slice. A dashed line shows a linear fit to the rising phase of this peak. Colored diamonds are the times at which the entire slice is plotted on the right panel. The first three diamonds correspond to the same times at which the entire ridge is sampled on the right of Figure 1. Triangles on the right panel mark half the peak value and are used to define the width of the bar. The axis along the right shows the lower bound on EM assuming peak emission from Fe XXIV. The FLARE2021 ridge (b) is sampled along a slice passing through the magenta diamond in Figure 4. The black curve is the EM, read on the left axis, and the green is the intensity, read on the right axis. The dashed line is a linear fit to the EM curve. The right panel shows slices at those times marked with diamonds on the intensity curve.

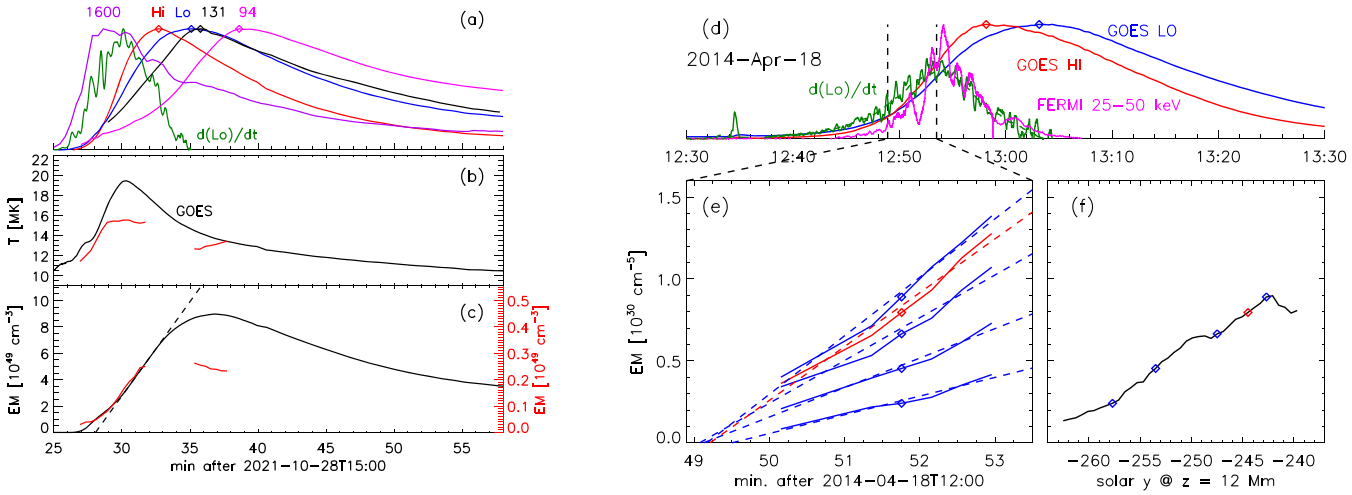

Figure 11. The time histories of FLARE2021 (a–c) and FLARE2014 (d–f). Normalized light curves are plotted in the upper panels, for FLARE2021 (a) and FLARE2014 (d), with GOES Hi (0.5–4 Å) in red and Lo (1–8 Å) in blue, and the derivative of Lo in green. Panel (a) shows light curves for FLARE2021 including total emission from 131 Å (black), 94 Å (magenta), and 1600 Å (violet), with peaks indicated by diamonds. The GOES channels are used to derive an overall temperature (b) and volume EM (c). Red curves show the values estimated for the ridge, with EM read from the right axis of (c). Panel (d), for FLARE2014, includes the light curve of 25–50 keV photons from the Fermi GBM (magenta). Panel (f) shows column EM along the ridge at 12:51:45 (see Figure 6), with diamonds calling out particular locations. Panel (e) shows the time evolution at each of those locations, with diamonds showing the time of panel (f).

time for 3–4 minutes. The dashed line in Figure 10(a) shows that the intensity of that particular point on FLARE2000 increases linearly, from which we place a lower bound $d(\mathrm{EM})/dt = 2.7 \times 10^{28}\,\mathrm{cm}^{-5}\,\mathrm{s}^{-1}$. Other points on the ridge are similarly well fit by linear increases, although with differing slopes. The point on the FLARE2021 ridge featured in Figure 10(b) shows an increase of $d(\mathrm{EM})/dt = 1.1 \times 10^{28}\,\mathrm{cm}^{-5}\,\mathrm{s}^{-1}$. FLARE2014, shown on figure 11(e), has rates varying along the ridge, up to $d(\mathrm{EM})/dt = 0.6 \times 10^{28}\,\mathrm{cm}^{-5}\,\mathrm{s}^{-1}$.

Figure 11 shows the linear phase in the context of the overall flare for those cases where the flare had a single, simple part: FLARE2021(a–c) and FLARE2014 (d–f). The HXR light curves of FLARE2014, Figure 11(d) were obtained by Fermi Gamma-ray Burst Monitor (GBM; Meegan et al. 2009) for the entire duration of the flare. It is shown that the ridge EM grows linearly while the HXR emission is increasing. The latter rises along with the time derivative of the GOES Lo channel (1–8 Å), following the well-known Neupert effect (Neupert 1968; Dennis & Zarro 1993; Veronig et al. 2002; Qiu 2021). The linear phase of FLARE2021 also occurs primarily during the rise in the GOES derivative (green curve in Figure 11(a)). The overall EM of the flare, derived using the two GOES channels (Figure 11(c)), rises in a similar manner. The volume EM of the entire ridge is estimated by assuming a width $w = 4$ Mm at

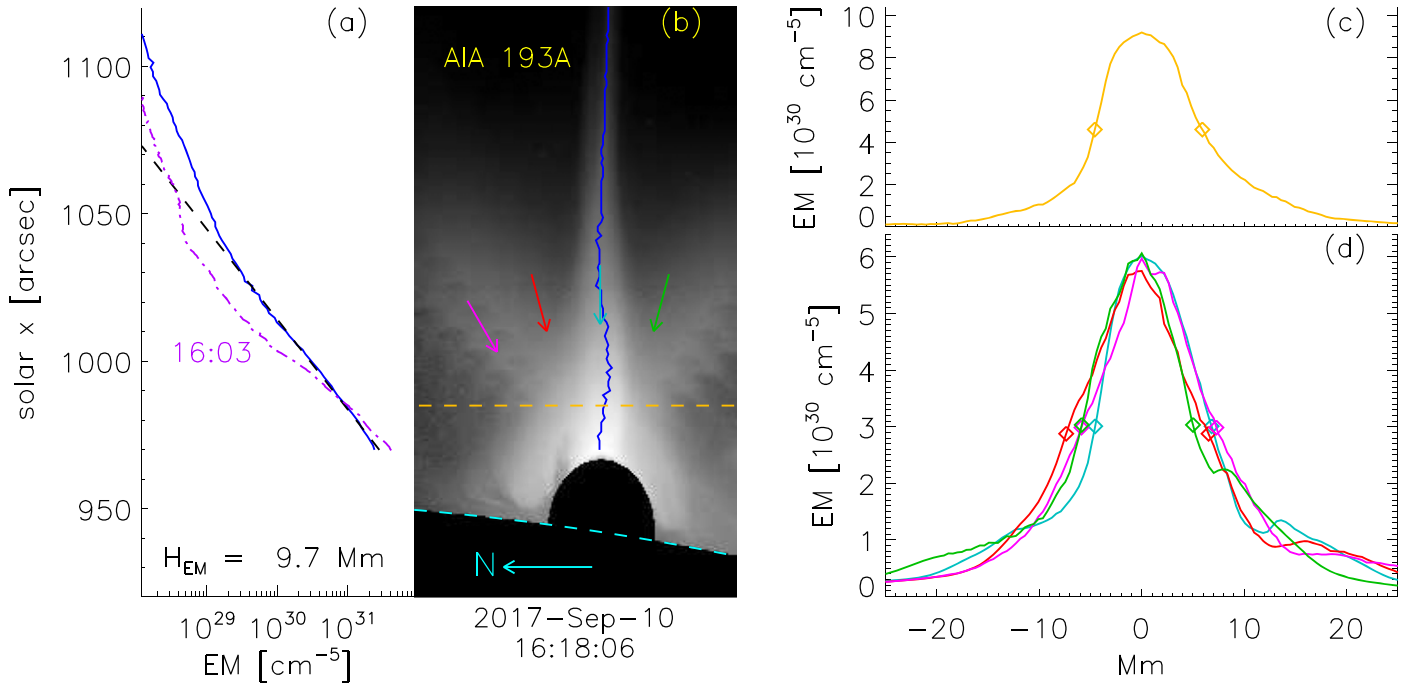

Figure 12. The plasma sheet above the flare 2017 September 10, i.e., SEPT10PS. (b) is an image from AIA 193 Å after the flare at 16:18, in logarithmic gray scale, with the disk and the arcade blacked out, and rotated to appear vertical. A blue curve shows the core of the plasma sheet, and the EM along this curve is plotted in blue to the left, in panel (a), along with an exponential fit (dashed) and the EM from an earlier time (16:03, violet broken line). A horizontal slice is indicated by an orange dashed line, and the EM along is plotted in panel (c). Four different viewpoints are indicated by colored arrows on panel (b). The EM integrated along each perspective is plotted in the matching color on panel (d). The value of EM assumes that panel (b) integrates along a line of sight $L_{\rm los} = 50$ Mm into the plane of the sky. Diamonds in (c) and (d) show the half maxima of each curve.

every pixel along the ridge (red curve against the right axis). This turns out to be only 5% of the flare's total. The flare's total EM has an approximately linear phase (dashed line) with $d(\mathrm{EM})/dt = 2.4 \times 10^{47}\,\mathrm{cm}^{-3}\,\mathrm{s}^{-1}$ beginning at 15:28:04 (the intercept of the dashed line). For reference, the column EM of the ridge pixel shown in Figure 10(b) begins its linear rise 18 s earlier at 15:27:46.

It is not easy to derive an electron density from the column EM, due to its steady increase over time. One estimate comes from using the peak value and assuming the column depth at that time equals the largest value of FWHM of the ridge (i.e assume $\Delta\ell \simeq w$ on Figure 7(a)). The peak value for FLARE2000, is $\mathrm{EM} \gtrsim 7 \times 10^{30}\,\mathrm{cm}^{-5}$, shown by the red diamond on Figure 10(a). This gives a lower bound on electron density $n_e = \sqrt{\mathrm{EM}/w} \gtrsim 1.5 \times 10^{11}\,\mathrm{cm}^{-3}$. FLARE2021 flare has a lower peak, $\mathrm{EM} = 2.6 \times 10^{30}\,\mathrm{cm}^{-5}$, and a wider ridge ($w = 4.1$ Mm) yielding a density estimate $n_e = \sqrt{\mathrm{EM}/w} = 0.8 \times 10^{11}\,\mathrm{cm}^{-3}$. The more complex geometry of FLARE2014 makes w more difficult to measure, although the width at 75%, $w = 3$ Mm, serves as a crude estimate. We return below to reconsider these density estimates in light of the linearly increasing EM.

4. Interpreting the Ridge

4.1. Proposed Relation to Supra-arcade Plasma Sheets

Supra-arcade plasma sheets, typified by SEPT10PS (see Figure 12(b)), are found to have densities and temperatures similar to those observed in ridges ($n_e \sim 10^{11}\,\mathrm{cm}^{-3}$, $T \sim$ 15–20 MK). It is therefore natural to propose that ridges are simply overhead views of vertical plasma sheets. This association seems problematic in light of plasma sheets' vertical extents: it would require a fortuitous perspective for a 100 Mm long sheet to appear as a ridge only ∼5 Mm wide. In point fact, emission originates primarily from very low in the plasma sheet, and viewpoint will not greatly affect its apparent width. Using the same simplified EM technique on SEPT10PS Longcope et al. (2018) derived the column EM plotted in blue in Figure 12(a). This falls off exponentially with a scale height of $H_{\rm EM} = 9.7$ Mm, as indicated by the dashed black line. We project the image, after removing the disk and the arcade (black regions in the figure), along lines of sight from four different perspectives, ranging from −15° to 30° from vertical, indicated by colored arrows. These different projections result in profiles shown in matching colors in Figure 12(d), all with very similar widths: FWHM ranging from 11 Mm (green) to 14 Mm (red). These widths are all comparable to a simple slice, whose FWHM is 10.5 Mm (Figure 12(c)). If we assume SEPT10PS is viewed along a column of $L_{\rm los} = 50$ Mm, then viewing from above would produce a ridge with column $\mathrm{EM} \simeq 6 \times 10^{30}\,\mathrm{cm}^{-5}$, comparable to that of FLARE2000. The peak EM from the different perspectives are all virtually identical.

We propose that the high-density ridge is an overhead view of the kind of vertical density concentration, which would appear as a plasma sheet when viewed edge on, as illustrated in Figure 7(a). The roughly linear increase in time of $\mathrm{EM} \simeq n_e^2 H_{\rm EM}$ must arise from either an increase in density, $n_e \sim t^{1/2}$, or from an increase in scale height $H_{\rm EM} \sim t$. Some evidence favoring the latter option is found in SEPT10PS. Performing the same analysis 15 minutes earlier, shown by the violet broken curve in Figure 12(a), yields an EM scale height of $H_{\rm EM} = 6.5$ Mm. The scale height is therefore exhibiting an average change of $\dot{H}_{\rm EM} = 4\ \mathrm{km\,s}^{-1}$, which does appear plausible, as we show below. Extrapolating backward at the same rate gives $H_{\rm EM} = 0$ at 15:35, a time not far from the time

of the eruption that triggered the flare (15:40, Seaton & Darnel 2018).

Our examples consist of high-density ridges early in the development of the plasma sheet. The syntheses illustrated in Figure 12 have ridge widths ($\sim H_{\rm EM} \simeq 10$ Mm) matching the width of the plasma sheet within its first scale height (see Figure 12(c)), but about double the width observed in our example ridges. Examples presented above are from the first 3–4 minutes of the flare, while well-developed plasma sheets appear somewhat later: Figure 12(b) shows the sheet 38 minutes after CME eruption. If the sheet grew at its mean rate, $\dot{H}_{\rm EM} = 4$ km s^{-1}, then $H_{\rm EM} \simeq 1$ Mm after 4 minutes. It is possible that its initial growth was somewhat faster, so that $H_{\rm EM}$ could be of order 4 Mm at that time. In this case, views from the same range of perspectives considered in Figure 12 would not lead to any broadening, and $w \simeq 4$ Mm. This interpretation is consistent with both the slow broadening ($\dot{w} \simeq 5.6$ km s^{-1}) exhibited by FLARE2000, and the southward deflection ($v_y \simeq -7.5$ km s^{-1}) observed in FLARE2014, discussed in Section 3.4.

Very strong evidence for our hypothesis could be provided by the observation from a second perspective, say one of the Solar TErrestrial RElations Observatory (STEREO; Kaiser et al. 2008) spacecraft, showing a plasma sheet above the location of an observed ridge. Unfortunately, there is no such observation in any of the cases we consider here. STEREO-A did have a view of the space above FLARE2014, but none of the Extreme Ultraviolet Imager (EUVI) 195 Å images show a plasma sheet. The ridge was located about 32° behind the STEREO-A limb, so only structures extending more than 125 Mm above the surface would be visible. Even the brightest plasma sheets, such as SEPT10PS, are very faint at such heights. Moreover, if the sheet were a plane extending vertically from the FLARE2014 ridge, it would be inclined 35° from the STEREO-A line of sight. This would probably render it too faint to observe even low down, and far less so at a height of 125 Mm. We do not, therefore, consider the absence of STEREO observations of a plasma sheet in this case to be evidence against our hypothesis.

Under the proposed association of the plasma sheet with the ridge, the sources of their high-density material are likely to be found above the ridge, rather than in evaporation from below it. We pursue this logic to interpret the ridge as the accumulation of coronal material moved down from a reconnection site above.

4.2. Downflows Building the Ridge

The overhead view provided by the ridge allows simultaneous characterization of the magnetic field and the rate of flare reconnection. Tracing the progress of the FLARE2021 flare ribbons across a magnetogram, as shown in Figure 13(c), provides a measurement of the reconnection electric field. The colored curves plotted over the HMI magnetogram move across the positive polarity of the region. Accurate coalignment with the HMI magnetogram is performed by plotting the $B_{\rm los} = \pm 75$ G contour over the 1600 Å image, and arranging for bright regions to be enclosed by contours. The velocity is found by computing the minimum distance between points on successive ribbons, assigning that distance to the point midway between them, and dividing by the interval. It is adjusted for projection and plotted using colors in Figure 13(b). The ribbon moves rapidly during the first 4 minutes, from 15:26:14 to about 15:30. Its speed is below 50 km s^{-1} to the left of $x = -25''$, and faster to the right.

The leading edge of the ribbon is taken to be the locus of coronal reconnection projected onto the chromospheric boundary. The ribbon speed, described above, gives the speed that the reconnection front progresses through a stationary plasma. The product of this speed and the local chromospheric field, gives the reconnection electric field, $E_{\rm rib} = |v_{\rm rib} B_{\rm rib}|$, plotted at different times in Figure 13(a). This can be interpreted as the rate, per unit length, at which magnetic flux is being reconnected (Forbes & Priest 1984; Poletto & Kopp 1986; Qiu et al. 2002). The electric field we compute follows the evolution of v relatively well, with the region left of $x = -25''$ peaking around $E = 250$ V m^{-1} at 15:28:26 (blue square) and decreasing thereafter. Reconnection to the right of that point appears stronger and more persistent.

We hypothesize that the ridge plasma is built up from the retraction of reconnected flux onto the arcade. Under that assumption, the rate at which the column $\Delta\ell$ grows is related to the rate at which reconnected flux piles up. There is no reliable way to measure the magnetic field within the plasma sheet, so we assume the strength at the sheet's base is similar to that of the extrapolated arcade below it, B_a (plotted along the top of Figure 4(b)). Nor can we determine its orientation, so we make the simplest assumption: the rate of total flux buildup per length, $E_a = |v_r B_a|$, matches that of the reconnection, $E_a = E_{\rm rib}$, but after a delay to account for retraction. Invoking these assumptions, and equating the downward flow to the upward buildup of the ridge, yields

$$\frac{d(\Delta\ell)}{dt} = \frac{E_a}{B_a} = \frac{E_{\rm rib}}{B_a} = \frac{|B_{\rm rib}|}{B_a}\,|v_{\rm rib}| \ . \tag{4}$$

We use the model arcade, shown in Figure 4(b), to map from the ribbon to the ridge, and equate $E_a = E_{\rm rib}$ using this mapping. The black curve of Figure 13(d) shows the electric field at 15:28:26 (i.e., the curve with the square in Figure 13(a)) mapped to the ridge. The red curve on that panel shows the inferred velocity, $d(\Delta\ell)/dt$. The time we consider, 15:28:26, is during the peak in ribbon motion, which occurs just before the ridge begins to grow. We propose that flux reconnected at that time reaches the arcade several minutes later to produce the rising EM. We, therefore, use the velocity plotted in Figure 13(d) to interpret the ridge. The value at the square, $d(\Delta\ell)/dt = 20$ km s^{-1}, would build to a total column $\Delta\ell = 5$ Mm, over the 4 minute interval of the linear rise shown in Figure 10(b); this is similar to the width of the ridge over that entire interval ($w = 4.1$ Mm).

Under our hypothesis, the column EM of the ridge increases steadily as the retracting flux arrives at the arcade. This causes the column length to increase steadily leading to a change $d({\rm EM})/dt = n_e^2\, d(\Delta\ell)/dt$, assuming the flux arrives with a plasma of a constant density. The evolving EM plotted along the top of Figure 4(a), or Figure 10(b), is fit to a line over the interval of 15:28:07–15:30:31 to obtain a measurement of $d({\rm EM})/dt$, plotted in Figure 13(e). This shows the same pair of peaks evident in the EM itself, and at the square it takes on the value of 1.1×10^{28} cm^{-5} s^{-1} matching the dashed line in Figure 10(b). The density of the ridge can then be computed from the ratio of Figures 13(d) and (e)

$$n_e = \sqrt{\frac{d({\rm EM})/dt}{d(\Delta\ell)/dt}} \ , \tag{5}$$

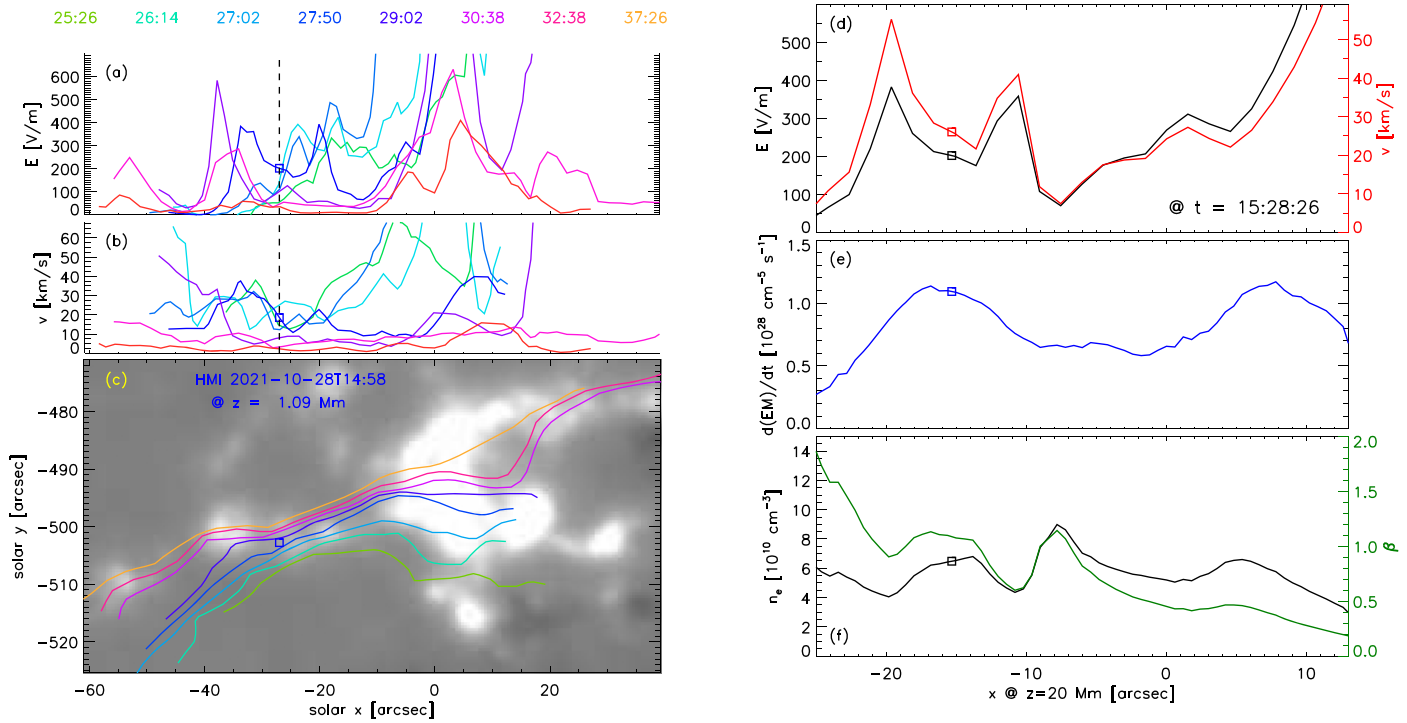

Figure 13. The motion of the positive (northern) flare ribbon (a–c) and its projection onto the ridge (d–f) for FLARE2021. (c) shows the leading edge of the AIA 1600 Å ribbon at different times, plotted in different colors, plotted over the line-of-sight field extrapolated to $z = 1.09$ Mm. The times represented by the different colors are listed along the top. (b) is the velocity of the ribbon computed at times between the ribbon positions in (c). (a) is the electric field, $E_{\rm rib} = |v_{\rm rib}B_{\rm rib}|$, from the motion of the ribbon and the extrapolated magnetic field. This field is mapped onto the ridge at $z = 20$ Mm as a black curve on (d), read against the left axis. The upward velocity, $d(\Delta\ell)/dt = E_{\rm rib}/B_a$, is plotted in red, read against the right axis. (e) is the rate of increase in the EM of the ridge, averaged over the period of linear increase shown in Figure 10(b) (15:28–15:31). (f) is the density inferred from Equation (5) using the ratio of (e) to (d). The green curve, read off the right axis, gives the local value of plasma β. Squares in all panels correspond to the position indicated by a magenta diamond in Figure 4 and analyzed in Figure 10(b), now translated to the time of the magnetogram. It is at the time in the middle of the ribbon motion: 15:28:26.

plotted in black in Figure 13(f). This takes on values $n_e \simeq 7 \times 10^{10}\,{\rm cm}^{-3}$, with a structure not entirely matching that found in $d({\rm EM})/dt$. This is close to the cruder estimate found by more conventional means in the previous section. Agreement is to be expected once we establish that the column grows to match the ridge width over 4 minutes. Equation (5) does, however, provide an estimate of n_e somewhat independent of the former. Their agreement can be taken as evidence in favor of the hypothesis that the ridge, and therefore the vertical sheet, is built by the accumulation of reconnected flux.

A final check is provided by estimating the local plasma β, using the plasma pressure, $p = 2n_e k_{\rm b} T$, where the temperature T is found from the simplified EM loci (see Figure 4(a)). Since we have no measurement of the magnetic field strength inside the ridge, we use the value from the top of the extrapolated arcade, plotted along the top of Figure 4(a). The result, shown by the green curve in Figure 13(f), read off the right axis, takes on values close to unity over the ridge, suggesting that the ridge plasma has pressure that can only just be confined by the magnetic field surrounding it. One must recall that the value of β reported compares internal plasma pressure to an estimate of *external* magnetic pressure.

4.3. Reconnection Energy Producing the Ridge

We repeat the foregoing computation for FLARE2014, but also use the Ultraviolet Footpoint Calorimeter (UFC; Qiu et al. 2012) to compute the energy released. For the purposes of the UFC, we use the entire light curve of each pixel in the AIA 1600 Å image, as shown in Figure 14(b). The successive peaks along a horizontal row of pixels are fit to obtain a velocity v_x. These values are plotted in blue in Figure 14(c). Each row of pixels is fit by one line over an interval of 12:37–13:00, providing a spatially resolved, time-averaged velocity, plotted in blue in Figure 14(c). This is used to compute a time-averaged electric field, $E_{\rm rib} = |v_{\rm rib}B_{\rm rib}|$, which is then mapped to the ridge at $z = 11.7$ Mm, along extrapolated field lines, and then divided by the apex field strength, B_a, according to Equation (4), to obtain the upward velocity $d(\Delta\ell)/dt$, plotted as a red line on Figure 14(c). Note that this is somewhat larger than the ribbon velocity (v at $z = 0$ in blue) because the ratio $B_a/B_{\rm rib}$ is generally less than unity. The use of the UFC velocity requires more spatial smoothing than tracking the ribbon front directly, so the curves in Figure 14(c) are smoother than that in Figure 13(b).

The EM of the FLARE2014 ridge is found using the simplified EM-loci method previously described. Its rate of change at different positions along the ridge, found from linear fits indicated by dashed lines in 11(e). The magenta diamond on Figure 14(d) falls on a point where $d({\rm EM})/dt = 0.45 \times 10^{28}\,{\rm cm}^{-5}\,{\rm s}^{-1}$, less than half the value highlighted for FLARE2021. The EM has a single maximum at the north end of the ridge, as seen before in Figures 6(a) and 11(f). The rate of change has this same shape because all points appear to begin growing around the same time (12:49, see figure 11(e)). The rate, $d({\rm EM})/dt$, is combined with the speed, $d(\Delta\ell)/dt$, through Equation (5) to compute the electron density plotted in Figure 14(e). Similar to the case of FLARE2021, the case

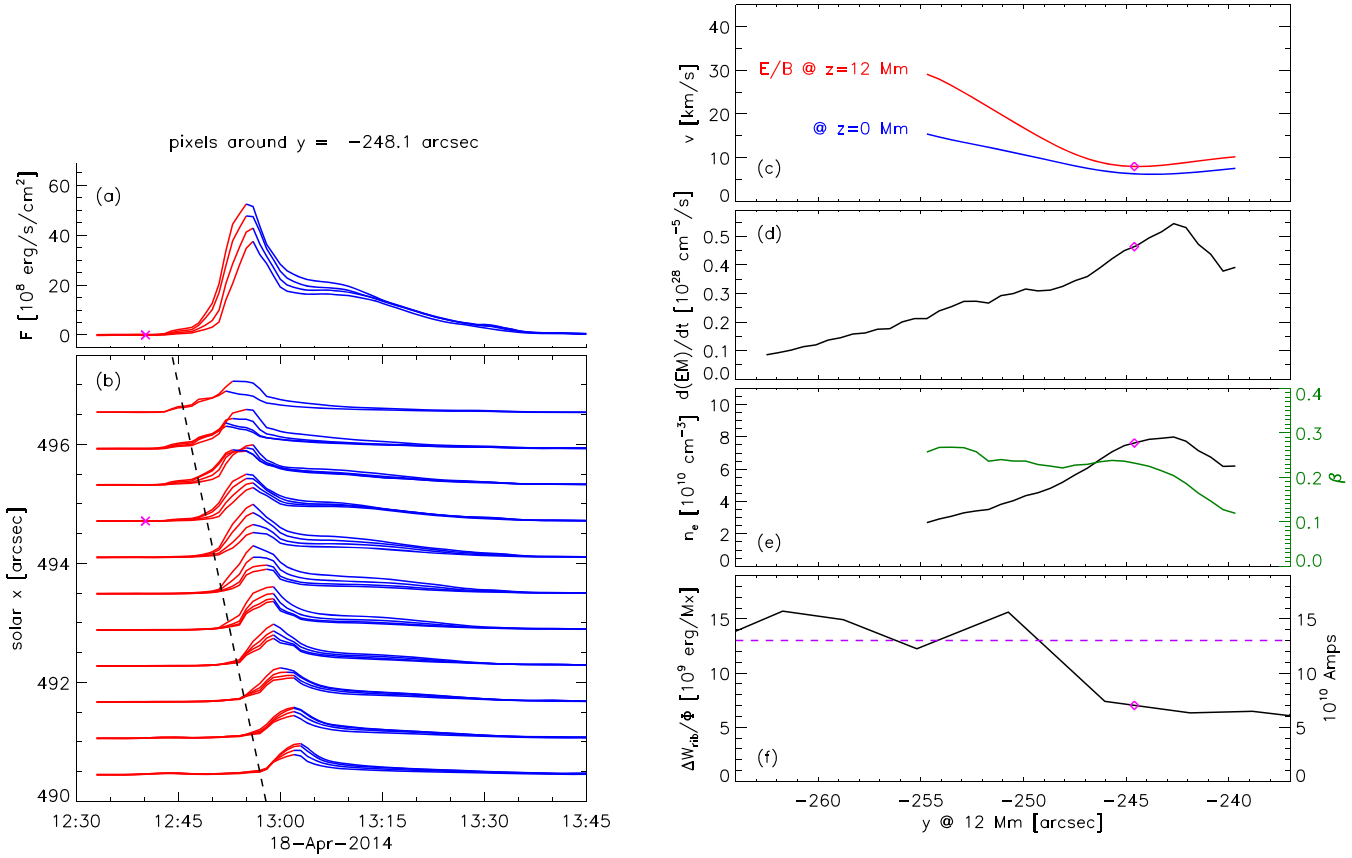

Figure 14. Ribbon velocity, reconnection electric field, and energy for FLARE2014. (b) shows AIA 1600 Å light curves, scaled intensity plotted vs. time, from pixels around the position $y = -248\farcs1$ (at $z = 0$ Mm), indicated by an arrow and magenta diamond in Figure 6 on the ridge ($z = 12$ Mm). Light curves from groups of pixels straddling that location at different horizontal coordinates are shown displaced so their location is read from the base level against the x-axis. A dashed line indicates the fit to the velocity, $v_x = -0\farcs54$. This corresponds to a speed of 7.8 km s^{-1} across the surface, after accounting for foreshortening. The rising phase of each light curve is plotted in red. (a) shows the heat flux, computed using the UFC, for pixel from $x = 494\farcs8$, indicated in (b) with a magenta ×. (c) is the velocity at the ribbon ($z = 0$ blue) mapped to the y coordinate along the ridge, and at the upward velocity of the ridge ($d(\Delta\ell)/dt$ red). (d) shows the time-averaged value $d(\mathrm{EM})/dt$ along the ridge. (e) combines (c) and (d) using Equation (5) to compute the density of downflowing material, in black read off the left axis. The green curve, read off the right axis, is the local plasma β. (f) is energy $\Delta W_{\rm rib}$ per unit flux. The left axis gives this in erg per maxwell, while the right axis converts this to amps. Magenta diamonds show the values at $y = -248\farcs1$, which is detailed in (a) and (b). The dashed horizontal line is the global average for the entire flare.

here peaks around $n_e \simeq 9 \times 10^{10}\,\mathrm{cm}^{-3}$. The estimate of plasma β, derived in the same way as above, is a bit below unity, therefore slightly smaller than for FLARE2021.

The UFC obtains an energy flux $F(t)$ by multiplying the 1600 Å light curve by an empirical factor λ (Qiu et al. 2012), as shown in Figure 14(a). The rising phase of the light curve is produced only by energy deposition into the chromosphere, while the declining phase includes a contribution from the cooling loop. We, therefore, integrate the rising portion of $F(t)$ and then double it to account for a declining phase, in order to estimate the total energy deposited from reconnection into that one footpoint. We double that value again, accounting for the conjugate footpoint, to obtain a net energy per area, $\Delta W_{\rm rib}$, sent downward from the corona. Dividing this by the local field strength, $B_{\rm rib}$, gives the energy per magnetic flux for each loop, plotted in black in Figure 14(f). Qiu (2021) applied the UFC to this entire flare and found $\Delta W_{\rm rib} = 2.7 \times 10^{31}$ erg and a total reconnected flux of $\Delta\Phi = 2.1 \times 10^{21}$ Mx, for a ratio of 13×10^9 erg Mx^{-1} plotted as a violet dashed line in Figure 14(f). It seems the southern section of the ribbon ($y < -250''$) is typical of the flare as a whole, while the northern section is characterized by half the averaged value.

5. Discussion

Analysis of three cases of high-density, high-temperature ridges observed during two-ribbon flares led us to the conclusion that these features are overhead views of the kind of vertical plasma sheets evident above other flares observed near the limb. Each ridge we observed shows a linear increase in column EM for about 3–4 minutes, beginning soon after the flare's onset. We have shown this to be consistent, qualitatively and quantitatively, with the accumulation of plasma at the base of the plasma sheet at a rate determined by the reconnection rate inferred from ribbon motion several minutes earlier. The density of accumulating plasma is found to be greatly enhanced above expected ambient coronal values, to $n_e \sim 8 \times 10^{10}$, which is similar to the values inferred in plasma sheets. Table 1 summarizes the properties of the ridges we have inferred from each case.

5.1. Can the Ridge be a Signature of FMTS or Evaporation Collision?

Several mechanisms routinely invoked to explain plasma density enhancement can be considered as the origin of the high density of the ridge. Reconnection outflow exceeding the

Table 1
Summary of the Properties of the Flare Ridges Observed and Derived in This Work

Flare	FLARE2000	FLARE2014	FLARE2021
Time	2000-07-14T10:30	2014-04-18T12:52	2021-10-28T15:30
Class	X6	M7	X1
Sky position	$(-50'', 240'')$	$(505'', -240'')$	$(0'', -530'')$
θ_c	14°	36°	33°
Ridge width w	3 Mm	3 Mm	4 Mm
T	…	17 MK	17 MK
max(EM)	7×10^{30} cm^{-5}	0.9×10^{30} cm^{-5}	2.5×10^{30} cm^{-5}
Arcade height h	26 Mm	12 Mm	20 Mm
$d(\mathrm{EM})/dt$	2.7×10^{28} cm^{-5} s^{-1}	0.6×10^{28} cm^{-5} s^{-1}	1.1×10^{28} cm^{-5} s^{-1}
$n_e = \sqrt{\mathrm{EM}/w}$	1.5×10^{11} cm^{-3}	0.5×10^{11} cm^{-3}	0.8×10^{11} cm^{-3}
E_{rib}	…	150 V m^{-1}	200 V m^{-1}
$d(\Delta\ell)/dt$	…	10 km s^{-1}	20 km s^{-1}
$n_e = \sqrt{\mathrm{EM}/\dot{\Delta\ell}}$	…	0.9×10^{11} cm^{-3}	0.7×10^{11} cm^{-3}

Note. Horizontal lines divide flare identifiers (top), quantities found directly from the data (middle), and properties of the ridge derived using a model (bottom).

fast-magnetosonic speed is expected to terminate at an FMTS, where the density would be enhanced (Forbes 1986; Aurass et al. 2002; Chen et al. 2015). While the ridge location matches that of an FMTS, other aspects of this mechanism do not favor it in this role. First, downflow speeds observed in SADs moving through plasma sheets are typically sub-Alfvénic and would not be expected to form an FMTS (Savage & McKenzie 2011; Longcope et al. 2018). Second, a compression ratio X would produce density $n_e = X\, n_{e,1}$ and field strength $B_a = XB_1$, where $n_{e,1}$ and B_1 are the pre-shock values. $d(\Delta\ell)/dt$ would need to match the upward speed of the shock, and the downward velocity above the FMTS would be $v_1 = (X+1)d(\Delta\ell)/dt$. Using the measured values of $d(\Delta\ell)/dt \sim 20$ km s^{-1}, gives $v_1 < 100$ km s^{-1}, comparable to that of SADs, but below expected Alfvén speeds. Moreover, the shock would raise T by more than X to its observed value of 15 MK, so pre-shock values would be below 10 MK. Plasma sheets, particularly SEPT10PS, have $T \sim 15$ MK similar to the ridge. Indeed, T appears to increase smoothly going downward, rather than abruptly at a shock.

High densities in flares are often attributed to evaporation, however, this may not hold for the plasma sheet or the ridge. Warren et al. (2018) use EIS and AIA data to measure elemental abundances in SEPT10PS, and concluded that the high-density plasma is of coronal rather than photospheric origin. This finding contrasts with the evaporation-collision mechanism proposed by Reeves et al. (2007) and Sharma et al. (2016) wherein the high loop-top density results from a shock formed between opposing jets of evaporation. The density enhancement expected from such shocks is not large enough to account for the ridge. Moreover, the shocks propagate away from the site of the collision, which should appear as an expansion of the ridge at close to the local speed of sound: $c_s \sim 650$ km s^{-1} at $T \simeq 15$ MK. The ridge of FLARE2000 is observed to expand at less than 1% of this speed ($\dot{w} \simeq 5.6$ km s^{-1}), while that of FLARE2014 does not expand at all.

When the flare loops have cooled, some exhibit bright knots at their apexes (see Figures 3(a) and 8(a)). These features are restricted to individual loops, and form a jagged line contrasting with the smooth, straight ridge. It is possible that these late-forming knots are the result of evaporation collision in the separate loops.

The most likely of the remaining mechanisms for ridge density enhancement is that it arises from a combination of Petschek-like SMSs, and compression during retraction. Longcope et al. (2018) model the dynamics of the flux retraction following reconnection in SEPT10PS. They find that slow magnetosonic shocks, coupled with retraction up a gradient in magnetic field strength, could produce densities with the observed magnitude and gradients. Their model does include chromospheric evaporation, but it is too slow and arrives too late to contribute to the plasma sheet. In accordance with a skewed-field Petschek model, a slow shock is formed from flows generated by flux retraction which are supersonic, though sub-Alfvénic. This heats the plasma to the kind of temperature, $T \sim 15$ MK, observed in the plasma sheet. These flows can persist even after the flux comes to rest at the top of the arcade (Longcope et al. 2016), adding longevity to the high-density source. By quantitatively relating the reconnection rate, observed via ribbon motion, to the increase in the ridge's column EM, the present study has provided further support for this scenario.

5.2. Relation of the Ridge to Other Features

We have proposed that ridges observed in two-ribbon disk flares are overhead views of structures that would appear as vertical plasma sheets if they were viewed on the limb. We used several lines of reasoning to make this association. It would be far more convincing if both phenomena were observed for a single flare from different perspectives. The EUVI imagers on STEREO offer the possibility of such a two-perspective observation, although none of our events qualified. Only for one (FLARE2014) was there any chance of seeing a plasma sheet, but we found none. In addition to alignment requirements for the ridge, observing a plasma sheet requires that the flare occurs close to the limb and that the length of the sheet line up with the line of sight. Neither of these conditions was satisfied by the FLARE2014 EUVI observation. A future study may be able to ascertain if these multiple conditions have ever been satisfied by an eruptive flare.

The late stages of the ridge may be related to another kind of loop-top feature from the literature. In observations of a limb flare on 2011 January 28 (SOL2011-01-28T01:03) by SDO/AIA and Hinode/XRT, Guidoni et al. (2015) identified

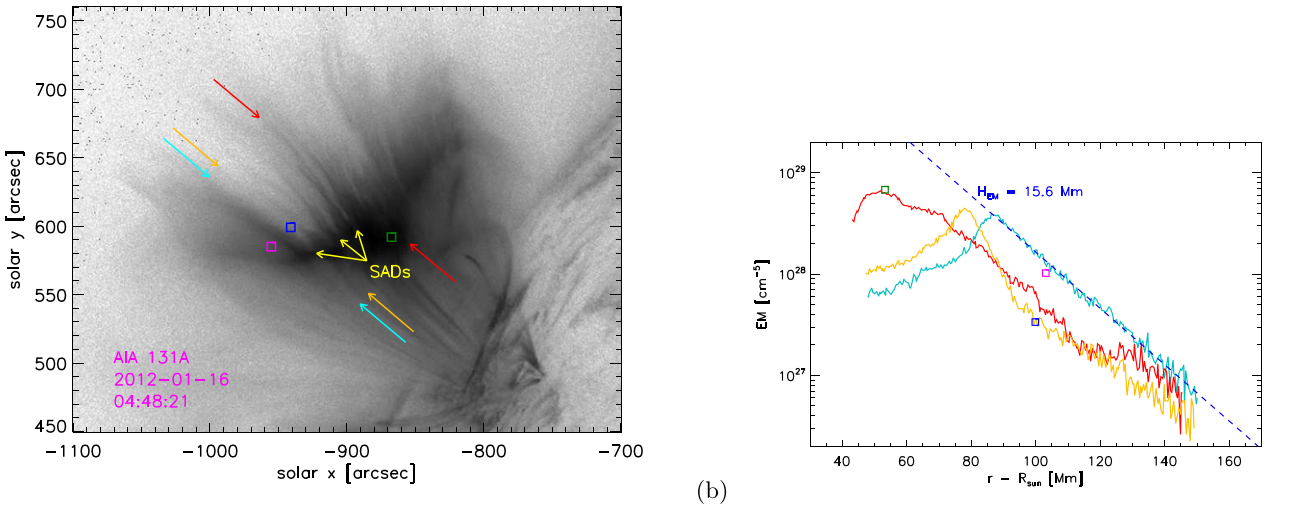

Figure 15. The fan above the flare on 2012 January 16. (a) is an image from AIA 131 Å, similar to Figure 15 in Hanneman & Reeves (2014), here plotted in inverse logarithmic gray scale. Colored squares show three points for which Hanneman & Reeves (2014) computed DEMs showing a hot, nearly isothermal component at $T \simeq 10$ MK. Colinear pairs of colored arrows indicate lines along which we compute the column EM under the assumption that $T = 10$ MK. Yellow arrows point to some examples of SADs moving through the fan array (they appear light in the inverse color scale). (b) plots the column EM for the points (squares) and lines (solid curves). One curve is fit to an exponential with $H_{\rm EM} = 15.6$ Mm.

a high-temperature, high-density, vertical structure at the loop apexes, that they dubbed a *tower*. It resembled structures previously seen at the tip of cuspy (or *candle-flame*) flares (Forbes & Acton 1996; Tsuneta 1996). The tower appeared in the flare's later phases, becoming visible about 30 minutes after onset and persisting at least another 30 minutes. In this particular flare, there did not appear to be a vertical extension of this structure resembling a more traditional plasma sheet. The temperature of the tower was found to be around ∼10 MK, and it appears most clearly in AIA 94 Å, 131 Å, and Hinode/XRT; these aspects are similar to the later phases of our ridge. Guidoni et al. (2015) found the density in the tower to be $n_e \simeq 10^{10}\,{\rm cm}^{-3}$ at the points of its peak brightness. Even in its late phase, our FLARE2021 ridge appears to have a density about 4 times higher than this (EM $= 10^{30}\,{\rm cm}^{-5}$ at 15:51:22, corresponds to a density of $n_e \simeq 5 \times 10^{10}\,{\rm cm}^{-3}$, using the line-of-site estimate of $w = 4$ Mm.).

The arcade of the tower event was observed from overhead in 195 Å, by EUVI on STEREO-A, but nothing resembling a ridge can be seen. This absence may be attributed to the lower density found in that particular flare. A few of the arcade loops visible in EUVI's 195 Å images appeared, however, to have loop-top knots at their apexes.

In some limb flares, the plasma sheet appears face-on as a hot, dense array of *fans* above the arcade (Švestka et al. 1998; Hanneman & Reeves 2014), such as the example in Figure 15(a). Warren et al. (1999) reported a diffuse layer of hot (15–20 MK) plasma above the arcade late in the flare of 1999 July 25, which could be the same structure. Notably, it is through these fans that SADs appear as dark, descending inclusions (indicated by yellow arrows in Figure 15(a)), which have been associated with flux tubes retracting following reconnection (McKenzie & Hudson 1999; Savage & McKenzie 2011). By studying the motion of the fan array itself, McKenzie (2013) concluded that its density was high enough that $\beta \gtrsim 1$.

The thorough investigation of Hanneman & Reeves (2014) provides preliminary evidence to associate the fan array with ridges and plasma sheets. They computed differential emission measures (DEMs) for SADs as well as points within the fan arrays of several flares. In one flare, 2012 January 16 (SOL2012-01-16T04:44), they computed DEMs within 4 minutes of the flare's peak. Their two fan points are indicated on the AIA 131 Å image in Figure 15(a) by green and magenta boxes, and their SAD point by a blue box. The DEMs they computed for those points include a high-temperature peak, $T \simeq 10$ MK, which we find to be extremely well fit to a narrow Gaussian ($\sigma_T \simeq 1.8$ MK). We use this fact to infer the column EM at those points (colored squares) and along lines indicated by pairs of colinear colored arrows in Figure 15(a). The column EMs, plotted in corresponding colors in Figure 15(b), each fall off approximately exponentially with $H_{\rm EM} \simeq 15.6$ Mm. The falloff of the fan (cyan) resembles at least one vertical plasma sheet (SEPT10PS with $H_{\rm EM} = 9.7$ Mm). The EM of the lower point, EM $\simeq 7 \times 10^{28}\,{\rm cm}^{-5}$, falls slightly below values in ridges, perhaps because the point is relatively high up ($z \simeq 55$ Mm), or because the column is given by the plasma sheet width rather than the scale height. In any event, we consider its EM and $H_{\rm EM}$ to be consistent with the hypothesis that a face-on fan array, an edge-on plasma sheet, and an overhead ridge, are all different views of the same structure.

Of the several SADs visible in Figure 15(a), Hanneman & Reeves (2014) selected one for DEM analysis. We identify this point with a blue square, and sample a line tracing the tail of the feature in orange. The column EM of the SAD here is EM $= 3.4 \times 10^{27}\,{\rm cm}^{-5}$, which is lower than the nearby fan by at least a factor of 3 (comparing blue to magenta squares). The column EM appears to fall off with a scale height similar to the fan. In light of its lower EM, we do not believe the SADs themselves would contribute emission to the ridge, if they were viewed from above. It is also possible that the EM plotted by the orange line in Figure 15(b) is from background material, and that the SAD's EM is even lower.

5.3. What the Ridges Reveal about Plasma Sheets

While the three instances of ridges we have studied lack a second perspective showing the plasma sheet above, we can use them to infer some properties that may apply to other

plasma sheet observations. The narrowness and straightness of the ridges help explain the surprising narrowness observed in plasma sheets. The ridges were straight enough that we estimated radii of curvature exceeding 1400 Mm (FLARE2000), and 200 Mm (FLARE2021), over distances of 30 Mm. If a plasma sheet were viewed edge on along the correct perspective, it would not appear broadened by curvature, and could retain a width comparable to that of the ridge: $w \sim 5$ Mm. The slightly larger width seen at the base of SEPT10PS ($w \sim 10$ Mm) may be due to a slight misalignment of perspective (6° over a length 50 Mm would increase the apparent width by 5 Mm) or simply to a ridge that is genuinely wider as considered above. Longcope et al. (2018) found SEPT10PS narrowed down to 4 Mm at a height of $z \simeq 100$ Mm, before expanding again to 10 Mm. This is consistent with a slight twist, say 6° over 100 Mm, rendering the viewpoint ideal at one particular height, and less so above and below. Finally, straightness over long line-of-sight distances, say over 30 Mm, is essential to explain the very large column EM seen in plasma sheets: EM $> 10^{31}$ cm^{-3} in SEPT10PS.

The ridge is even straighter than the smooth magnetic model we use (compare to the magenta curve in Figure 7(b)). This points to an effect of magnetic tension from a guide-field component in the field surrounding the plasma sheet. Indeed, the hints of hot loops discussed in Section 3.3, cross the ridge at angles suggesting a guide-field component comparable to the strength of the underlying arcade. In this way, it seems that dense ridges provide some insight into the magnetic structure of the CSs that nucleate them.

The time evolution of the ridge provides new insight into the timing of plasma sheet formation. The linear rise in its EM indicates that ridge formation begins simultaneously along its length, during the flare's earliest phase. The simultaneity is particularly evident in Figure 11(e), where five points along the FLARE2014 ridge fit linear functions of t with almost the same start time, 12:49. The 25–50 keV emission from Fermi/GBM, grows linearly with a start time 1 minute earlier, at 12:48. (This is an extrapolation of the linear growth; HXR emission actually begins even earlier.) The HXR and the GOES derivative both peak 5 minutes later, at 12:54, after the ridge has stopped increasing. So the ridge forms steadily between the beginning and peak of HXR emission.

The delay between onsets of HXR and ridge emission opens the possibility that evaporation plays some role in ridge formation. The loop selected in Figure 6(b) (violet) has a full length of $L = 40$ Mm, so evaporation at 350 km s^{-1} could reach its apex during the 1 minute delay. Since 350 km s^{-1} would be subsonic (if $T > 4$ MK) or mildly supersonic (if $1 < T < 4$ MK), strong density enhancement still requires a shock other than from traditional evaporation collision. It is possible that the upward, subsonic evaporation passes through the downward propagating rotational discontinuity of the reconnection outflow to become accelerated and then strongly shocked at an SMS. Such possible interplay between evaporation and reconnection needs more investigation before we can hope to understand signatures like the ridge and the plasma sheet.

Our analysis of ridges may also provide insight into the supra-arcade fans and SADs descending through them. The values of β we report in Figures 13 and 14 compare the internal plasma pressure to a measure of external magnetic pressure, and are therefore not directly comparable to those reported by McKenzie (2013). To maintain pressure balance, the internal magnetic field strength would need to be lower than the external, making the actual β greater than unity, in agreement with McKenzie (2013). If the ridge is an overhead view of a fan array, then both the SADs and the surrounding plasma they move through would be manifestations of flux retraction following reconnection. SADs would constitute a subset of retracting flux tubes distinguished by their lower density (Hanneman & Reeves 2014). It is possible that the scenario for evaporation interaction, crudely described above, is not active in every flux tube, leaving a select few to retain lower density and appear as SADs.

The ridge cools gradually and remains visible long beyond the phase of magnetic reconnection indicated by the outward motion of flare ribbons. The ridge of FLARE2021, cools from 16 to 5 MK over 30 minutes, appearing in progressively cooler bands as it does so. This level of persistence is also seen in SEPT10PS, which remains visible above the limb, with the classic CS configuration, for over 2 hr (Longcope et al. 2018). The overhead perspective shows that the cooling ridge exists long beyond the classic flare ribbon motion. The ribbon of FLARE2021 remains visible in 1600 Å beyond 16:00, but organized brightening of new ribbon pixels ends at 15:42. Anomalously slow cooling of flare loops, and their footpoints, has been attributed to some form of extended heating, active beyond their creation by reconnection (Qiu & Longcope 2016; Zhu et al. 2018). It is possible that this same mechanism is responsible for the persistence of the ridge. This provides evidence that the unspecified extended heating mechanism is active within the plasma sheet.

5.4. Why Every Flare Does Not Show a Ridge

This study confined its consideration to three selected examples of flares exhibiting high-density ridges. Two of these (FLARE2000 and FLARE2021) showed very clear ridges, while the ridge on the third (FLARE2014) was not as obvious. There are undoubtedly many other examples of this phenomenon, however, not every two-ribbon flare shows a ridge of emission from Fe XXIV between its ribbons. The particular conditions that made our cases apparent cannot be expected in every flare. A vertical CS is the first condition, and it is not obvious that every flare, even every eruptive flare, harbors one of these. The sheet's vertical and the line of sight need to be closely aligned, although perhaps not as closely as might have been originally expected: $\lesssim 35°$ appears sufficient. Of the three ridges we considered, the clearest appeared at 14° (FLARE2000) and 33° (FLARE2021) from the disk center, while FLARE2014, at 36°, was not as obvious. In addition, the sheet plasma must have a temperature falling in the range of $15 < T < 20$ MK for AIA 193 Å to reveal the kind of ridge we have studied here. Hotter sheets may be possible, but would not appear in 193 Å. In light of these factors, it seems that we should not expect ridges to be ubiquitous; they are not.

The appearance and visibility of ridges may be somehow related to the size of the flare, among other factors. All three of our cases have GOES classifications above M5, and the weakest of them (FLARE2014, at M7) is also the one with the least pronounced ridge. Since it is based on X-ray brightness, the GOES classification primarily reflects the density of hot plasma in the flare, typically attributed to evaporation. Even though the ridges may not be directly related to evaporation themselves, the higher densities in X-class flares might make them more likely to host such high-density features. Indeed, the

values of EM and $d(\mathrm{EM})/dt$ for the three ridges, correlate with the GOES class (see Table 1).

Our reconnection hypothesis suggests that flares with relatively straight, parallel ribbons are also more likely to exhibit vertical plasma sheets that would appear as ridges. It is notable that the flare with the least straight and parallel ribbons, namely, FLARE2014, exhibits the least obvious ridge. Much would be learned from a thorough study of the frequency of ridges among two-ribbon, X-class flares.

We thank K. Reeves for discussions about these particular ridges, and A. Takeda for help with the XRT analysis. We thank the anonymous referee for suggestions that helped improve the manuscript. This work is supported by a NASA HSO-Connect grant and NASA grant No. 80NSSC19K0269. SDO is a mission of NASA's Living With a Star Program.

ORCID iDs

Jiong Qiu https://orcid.org/0000-0002-2797-744X

References

Antonucci, E., & Dennis, B. R. 1983, SoPh, 86, 67
Aschwanden, M. J., & Alexander, D. 2001, SoPh, 204, 91
Aurass, H., Vršnak, B., & Mann, G. 2002, A&A, 384, 273
Brannon, S. R., Longcope, D. W., & Qiu, J. 2015, ApJ, 810, 4
Brosius, J. W., & Daw, A. N. 2015, ApJ, 810, 45
Brosius, J. W., Daw, A. N., & Inglis, A. R. 2016, ApJ, 830, 101
Caspi, A., & Lin, R. P. 2010, ApJ, 725, L161
Chen, B., Bastian, T. S., Shen, C., et al. 2015, Sci, 350, 1238
De Pontieu, B., Title, A. M., Lemen, J. R., et al. 2014, SoPh, 289, 2733
Deng, G. 2011, ITIP, 20, 1249
Dennis, B. R., & Zarro, D. M. 1993, SoPh, 146, 177
Doschek, G. A., Warren, H. P., Harra, L. K., et al. 2018, ApJ, 853, 178
Fisher, G. H. 1989, ApJ, 346, 1019
Fletcher, L., & Hudson, H. 2001, SoPh, 204, 69
Forbes, T. G. 1986, ApJ, 305, 553
Forbes, T. G. 2000, JGR, 105, 23153
Forbes, T. G., & Acton, L. W. 1996, ApJ, 459, 330
Forbes, T. G., & Priest, E. R. 1984, in Solar Terrestrial Physics: Present and Futures, ed. D. Butler & K. Papadopoulos, Vol. 35 (Washington, DC: NASA)
Freeland, S. L., & Handy, B. N. 1998, SoPh, 182, 497
Gary, D. E., Chen, B., Dennis, B. R., et al. 2018, ApJ, 863, 83
Golub, L., et al. 2007, SoPh, 243, 63
Graham, M. L., Sand, D. J., Zaritsky, D., & Pritchet, C. J. 2015, ApJ, 807, L22
Guidoni, S. E., McKenzie, D. E., Longcope, D. W., Plowman, J. E., & Yoshimura, K. 2015, ApJ, 800, 54
Handy, B. N., Acton, L. W., Kankelborg, C. C., et al. 1999, SoPh, 187, 229
Hanneman, W. J., & Reeves, K. K. 2014, ApJ, 786, 95
Innes, D. E., McKenzie, D. E., & Wang, T. 2003, SoPh, 217, 247
Jiang, Y. W., Liu, S., Liu, W., & Petrosian, V. 2006, ApJ, 638, 1140
Kaiser, M. L., Kucera, T. A., Davila, J. M., St+, et al. 2008, SSRv, 136, 5
Kosugi, T., Sakao, T., Masuda, S., et al. 1994, in Proc. of Kofu Symp. 127 (Nagano: Nobeyama Radio Observatory), 127
Landi, E., Feldman, U., & Dere, K. P. 2002, ApJ, 574, 495
Lemen, J. R., Title, A. M., Akin, D. J., et al. 2012, SoPh, 275, 17
Li, Y., Ding, M. D., Qiu, J., & Cheng, J. X. 2015, ApJ, 811, 7
Li, Y., Xue, J. C., Ding, M. D., et al. 2018, ApJL, 853, L15
Lin, R. P., Dennis, B. R., Hurford, G. J., et al. 2002, SoPh, 210, 3
Lin, R. P., Potter, D. W., Gurnett, D. A., & Scarf, F. L. 1981, ApJ, 251, L109
Lin, Y., & Lee, L. C. 1999, PhPl, 6, 3131
Liu, W.-J., Qiu, J., Longcope, D. W., & Caspi, A. 2013, ApJ, 770, 111
Longcope, D., Unverferth, J., Klein, C., McCarthy, M., & Priest, E. 2018, ApJ, 868, 148
Longcope, D. W. 2014, ApJ, 795, 10
Longcope, D. W., Des, J., Des Jardins, A. C., Carranza-Fulmer, T., & Qiu, J. 2010, SoPh, 267, 107
Longcope, D. W., & Guidoni, S. E. 2011, ApJ, 740, 73
Longcope, D., Qiu, J., & Brewer, J. 2016, ApJ, 833, 211
Masuda, S., Kosugi, T., Hara, H., Tsuneta, S., & Ogawara, Y. 1994, Natur, 371, 495
McKenzie, D. E. 2013, ApJ, 766, 39
McKenzie, D. E., & Hudson, H. S. 1999, ApJ, 519, L93
McKenzie, D. E., & Savage, S. L. 2009, ApJ, 697, 1569
McTiernan, J. M., Fisher, G. H., & Li, P. 1999, ApJ, 514, 472
Meegan, C., et al. 2009, ApJ, 702, 791
Milligan, R. O., & Dennis, B. R. 2009, ApJ, 699, 968
Neupert, W. M. 1968, ApJL, 153, L59
Patsourakos, S., Antiochos, S. K., & Klimchuk, J. A. 2004, ApJ, 614, 1022
Petschek, H. E. 1964, in AAS-NASA Symp. on the Physics of Solar Flares, ed. W. N. Hess (Washington DC: NASA), 425
Poletto, G., & Kopp, R. A. 1986, in The Lower Atmospheres of Solar Flares, ed. D. F. Neidig (Sunspot, NM: National Solar Observatory), 453
Polito, V., Dudík, J., Kašparová, J., et al. 2018a, ApJ, 864, 63
Polito, V., Galan, G., Reeves, K. K., & Musset, S. 2018b, ApJ, 865, 161
Qiu, J. 2021, ApJ, 909, 99
Qiu, J., Lee, J., Gary, D. E., & Wang, H. 2002, ApJ, 565, 1335
Qiu, J., Liu, W.-J., & Longcope, D. W. 2012, ApJ, 752, 124
Qiu, J., & Longcope, D. W. 2016, ApJ, 820, 14
Reeves, K. K., Warren, H. P., & Forbes, T. G. 2007, ApJ, 668, 1210
Savage, S. L., & McKenzie, D. E. 2011, ApJ, 730, 98
Savage, S. L., McKenzie, D. E., Reeves, K. K., Forbes, T. G., & Longcope, D. W. 2010, ApJ, 722, 329
Scherrer, P. H., Bogart, R. S., Bush, R. I., et al. 1995, SoPh, 162, 129
Scherrer, P. H., Schou, J., Bush, R. I., et al. 2012, SoPh, 275, 207
Seaton, D. B., Bartz, A. E., & Darnel, J. M. 2017, ApJ, 835, 139
Seaton, D. B., & Darnel, J. M. 2018, ApJL, 852, L9
Sharma, R., Tripathi, D., Isobe, H., & Ghosh, A. 2016, ApJ, 823, 47
Sheeley, N. R., Jr, Warren, H. P., & Wang, Y.-M. 2004, ApJ, 616, 1224
Soward, A. M. 1982, JPlPh, 28, 415
Švestka, Z., Fárník, F., Hudson, H. S., & Hick, P. 1998, SoPh, 182, 179
Tsuneta, S. 1996, ApJ, 456, L63
Unverferth, J., & Longcope, D. 2018, ApJ, 859, 170
Veronig, A., Vršnak, B., Dennis, B. R., Temmer, M., Hanslmeier, A., & Magdalenić, J. 2002, A&A, 392, 699
Veronig, A. M., Brown, J. C., Dennis, B. R., Schwartz, R. A., Sui, L., & Tolbert, A. K. 2005, ApJ, 621, 482
Veronig, A. M., Karlický, M., Vršnak, B., et al. 2006, A&A, 446, 675
Warren, H. P., Bookbinder, J. A., Forbes, T. G., et al. 1999, ApJ, 527, L121
Warren, H. P., Brooks, D. H., Ugarte-Urra, I., et al. 2018, ApJ, 854, 122
Zhu, C., Qiu, J., & Longcope, D. W. 2018, ApJ, 856, 27